

Gastão Davanzo Gustavo (Orcid ID: 0000-0002-6723-1933)
de Souza Filho Antonio Francisco Souza (Orcid ID: 0000-0003-4728-1228)
Peron Jean Pierre Schatzmann (Orcid ID: 0000-0003-1638-8866)

SARS-CoV-2 Infection Impacts Carbon Metabolism and Depends on Glutamine for Replication in Syrian Hamster Astrocytes

Lilian Gomes de Oliveira^{1,2+}, Yan de Souza Angelo^{1,2+}, Pedro Yamamoto^{1,2}, Victor Corasolla Carregari³, Fernanda Crunfli³, Guilherme Reis-de-Oliveira³, Lícia Costa³, Pedro Henrique Vendramini³, Érica Almeida Duque⁴, Nilton Barreto dos Santos^{4*}, Egidi Mayara Firmino⁵, Isadora Marques Paiva⁵, Glaucia Maria Almeida⁶, Adriano Sebollela⁶, Carolina Manganeli Polonio^{1,2}, Nagela Ghabdan Zanluqui^{1,2}, Marília Garcia de Oliveira¹, Patrick da Silva^{1,2}, Gustavo Gastão Davanzo⁷, Marina Caçador Ayupe⁸, Caio Loureiro Salgado⁸, Antônio Francisco de Souza Filho⁹, Marcelo Valdemir de Araújo⁹, Taiana Tainá Silva-Pereira⁹, Angélica Cristine de Almeida Campos¹⁰, Luiz Gustavo Bentim Góes¹⁰, Marielton dos Passos Cunha¹⁰, Elia Garcia Caldini¹¹, Maria Regina D'Império Lima¹², Denise Moraes Fonseca⁸, Ana Márcia de Sá Guimarães⁹, Paola Camargo Minoprio¹⁰, Carolina Demarchi Munhoz⁴, Cláudia Madalena Cabrera Mori¹³, Pedro Manoel Moraes-Vieira⁷, Thiago Mattar Cunha⁵, Daniel Martins-de-Souza^{3,14,15,16,#}, Jean Pierre Schatzmann Peron^{1,2,17,#}.

¹ Neuroimmune Interactions Laboratory, Institute of Biomedical Science, Department of Immunology, University of São Paulo, São Paulo, SP, Brazil CEP 05508-000.

² Neuroimmunology of Arboviruses Laboratory, Scientific Platform Pasteur, University of São Paulo, São Paulo, SP, Brazil CEP 05508-020.

³ Laboratory of Neuroproteomics, Department of Biochemistry and Tissue Biology, Institute of Biology, University of Campinas (UNICAMP), Campinas, SP, Brazil CEP 130838-62.

This article has been accepted for publication and undergone full peer review but has not been through the copyediting, typesetting, pagination and proofreading process which may lead to differences between this version and the [Version of Record](#). Please cite this article as doi: [10.1111/jnc.15679](https://doi.org/10.1111/jnc.15679)

This article is protected by copyright. All rights reserved.

⁴ Department of Pharmacology, Institute of Biomedical Sciences, University of São Paulo, São Paulo, Brazil CEP 05508-000.

⁵ Center for Research in Inflammatory Diseases (CRID); Department of Pharmacology - Ribeirão Preto Medical School - University of São Paulo, Ribeirão Preto, Brazil CEP 14048-900.

⁶ Department of Biochemistry and Immunology, Ribeirão Preto Medical School, University of São Paulo, Ribeirão Preto, Brazil. CEP 01448-900.

⁷ Laboratory of Immunometabolism, Department of Genetics, Evolution, Microbiology and Immunology, Institute of Biology, University of Campinas, Campinas, Brazil CEP 130838-62.

⁸ Laboratory of Mucosal Immunology, Department of Immunology - Institute of Biomedical Sciences, University of São Paulo, São Paulo, Brazil CEP 05508-000.

⁹ Laboratory of Applied Research in Mycobacteria, Department of Microbiology, Institute of Biomedical Sciences, University of São Paulo, São Paulo, SP, Brazil CEP 05508-000.

¹⁰ Scientific Platform Pasteur - USP, University of São Paulo, São Paulo, SP, Brazil CEP 05508-020.

¹¹ Laboratory of Cellular Biology (LIM 59), School of Medicine, University of São Paulo, São Paulo, SP CEP 01246-903 Brazil.

¹² Department of Immunology, University of São Paulo, São Paulo, SP, Brazil CEP 05508-000.

¹³ Department of Pathology, School of Veterinary Medicine and Animal Science, University of São Paulo, São Paulo, SP, Brazil CEP 05508-270.

¹⁴ Experimental Medicine Research Cluster (EMRC), University of Campinas, Campinas, SP, Brazil CEP 13083-862.

¹⁵ D'Or Institute for Research and Education (IDOR), São Paulo, SP, Brazil CEP 04502-001.

¹⁶ Instituto Nacional de Biomarcadores em Neuropsiquiatria (INBION), Conselho Nacional de Desenvolvimento Científico e Tecnológico, São Paulo, SP, Brazil CEP 05303-903.

¹⁷ Immunopathology and Allergy Post Graduate Program, School of Medicine, University of São Paulo, São Paulo, SP CEP 01246-903 Brazil.

+ These authors contributed equally to this work.

**In memoriam* of a great scientist and human being that lost the battle against COVID-19.

Correspondence to:

Jean Pierre Schatzmann Peron

Address: Prof. Lúcio Martins Rodrigues, 370 BIA 4 Andar - Cidade Universitária, São Paulo, SP, Brazil. CEP 05508-020.

Daniel Martins de Souza

Address: Rua Monteiro Lobato, 255 Cidade Universitária Zeferino Vaz Campinas, SP CEP 13083-862.

A preprint version of this manuscript was posted on bioRxiv on 24 October, 2021:

<https://doi.org/10.1101/2021.10.23.465567>.

Abbreviations List	
2-Amino-2-hydroxymethyl-propane-1,3-diol	TRIS
2-deoxy-D-Glucose-6-phosphate	2-DG
2,2',2'',2'''-(Ethane-1,2-diylidinitrilo)tetraacetic acid	EDTA
4-aminobutanoic acid	GABA
4',6'-diamidino-2-phenylindole	DAPI
6-diazo-5-oxo-L-nor-Leucine	DON
Acetonitrile	ACN
Acetonitrile	CAN
Ammonium Hydroxide	NH ₄ OH
Ammonium acetate	NH ₄ CHOO
Amyotrophic Lateral Sclerosis	ALS
Angiotensin Converting Enzyme-carnitine palmitoyltransferase 1a	ACE-2 CPT-1a
Charge	Z
Chloroform	HCCI
Complementary Desoxy-Ribonucleic Acid	cDNA
COVID-19	Coronavirus Disease 2019
Cycle Threshold	Ct
Cytomegalovirus	CMV
Data-independent acquisition	DIA
Days post infection	dpi
Days post partum	dpp
Desoxy-Ribonucleic Acid	DNA
Differentially expressed protein	DEP
Dorso-lateral prefrontal cortex	DLPFC
Dulbecco's Modified Eagle Medium	DMEM
Envelope	E
Etomoxir	ETO
Exact Mass Retention Time	EMRT
False Discovery Rate	FDR
Fast Adaptive and Secure	FASP

Fetal Bovine Serum	FBS
Herpes Simplex Virus	HSV
Hours post infection	hpi
Human Immunodeficiency Virus	HIV
Huntington Disease	HD
Hydrophobic Interaction Liquid Chromatography	HILIC
Institute of Biomedical Sciences	ICB
Interferon	IFN
Interferon-Stimulated Gene	ISG
Interleukin	IL
Kyoto Encyclopedia of Genes and Genomes	KEGG
Liquid Chromatography	LC
Magnetic resonance imaging	MRI
Mass	M
Mass Spectrometry	MS
Median Tissue Culture Infectious Dose	TCID50
Melanoma differentiation-associated protein 5	MDA-5
Membrane	M
Methanol	MeOH
Mitochondrial Glutaminase	GLS
Multiplicity of Infection	MOI
Non-essential amino acids	NEAA
Nucleocapsid	N
Olfactory Sensory Neurons	OSN
Open Reading Frame	ORF
Paraformaldehyde	PFA
Phosphate Saline Buffer	PBS
Plaque Forming Units	PFU
Post-Acute Sequelae of COVID-19	PASC
Principal Component Analysis	PCA
Programmed Cell Death protein 1	PD-1
Quantitative Real Time Polymerase Chain Reaction	RT-qPCR
Retinoic Acid-Inducible Gene I	RIG-I
Ribonucleic Acid	RNA
Severe acute respiratory syndrome	SARS
Scientific Platform Pasteur-USP	SPPU
Single nuclei RNA sequencing	snRNA-seq
Spike	S

Sub-genomic RNA	sgRNA
T-cell immunoglobulin and mucin-domain containing-3	TIM-3
Transmembrane Protease Serine 2	TMPRSS2
Transmission Electron Microscopy	TEM
Tricarboxylic Acid Cycle	TCA
Tumor Necrosis Factor alpha	TNF-a
Ultra-Performance Liquid Chromatography	UPLC
Uniform Manifold Approximation and Projection	UMAP
University of São Paulo	USP
Vesicular Glutamate Transporters	vGLUT
Water	H2O
World Health Organization	WHO

ABSTRACT

COVID-19 causes more than million deaths worldwide. Although much is understood about the immunopathogenesis of the lung disease, a lot remains to be known on the neurological impact of COVID-19. Here we evaluated immunometabolic changes using astrocytes *in vitro* and dissected brain areas of SARS-CoV-2 infected Syrian hamsters. We show that SARS-CoV-2 alters proteins of carbon metabolism, glycolysis, and synaptic transmission, many of which are altered in neurological diseases. Real-time respirometry evidenced hyperactivation of glycolysis, further confirmed by metabolomics, with intense consumption of glucose, pyruvate, glutamine, and alpha ketoglutarate. Consistent with glutamine reduction, the blockade of glutaminolysis impaired viral replication and inflammatory response *in vitro*. SARS-CoV-2 was detected *in vivo* in hippocampus, cortex, and olfactory bulb of intranasally infected animals. Our data evidence an imbalance in important metabolic molecules and neurotransmitters in infected astrocytes. We

suggest this may correlate with the neurological impairment observed during COVID-19, as memory loss, confusion, and cognitive impairment.

Keywords: SARS-CoV2, COVID-19, neuropathology, glutamine, proteomics.

INTRODUCTION

Human coronaviruses are enveloped 30Kb single-stranded (+)RNA viruses and the causative agent of common cold and severe acute respiratory syndrome (SARS). Six members of the *coronaviridae* family are capable of infecting humans, considered of low (HCoV 229E, HCoV NL63, HCoV HKU1 and CoV OC43) or high (SARS-CoV, MERS-CoV and SARS-CoV2) pathogenicity (Audi *et al.* 2020). SARS-CoV-2 pandemic started in December 2019 in Wuhan, China after the probable spill over from bats due to mutations of the spike proteins (Wu *et al.* 2020; Guan *et al.* 2020).

Mild disease is observed in most patients, who develop fever, headache, and coughing. Some patients, however, evolve to severe acute respiratory syndrome (SARS), characterized by lung inflammation with intense myeloid cellular inflammatory infiltrate, hyaline membrane formation and alveolitis, clearly evidenced by lung magnetic resonance imaging (MRI) (Wu *et al.* 2020; Zhou *et al.* 2020; Barton *et al.* 2020). This results in dyspnea, difficult breathing, and low oxygen saturation. Most severe cases evolve with cytokine storm and systemic organ failure (Lu *et al.* 2020), mainly in people with comorbidities such as hypertension, obesity, and diabetes, probably due to either altered immune responses (Bastard *et al.* 2020; Witkowski *et al.* 2021) or to the higher expression of Angiotensin Converting Enzyme-2 (ACE-2) in the lungs (Pinto *et al.* 2020). Since January 30th, 2020, when the WHO declared a state of emergency and international concern, more than 6.2 million people died of COVID-19.

Viral particles invade host cells using its Receptor Binding Domain (RBD) of the spike protein through the interacting with ACE-2 expressed mostly on type II pneumocytes but also on other cell types, including endothelial cells, astrocytes, enterocytes and many others (Chu *et al.* 2021; Chen *et al.* 2021). Further, spike is cleaved in subunits S1 and S2 by the protease Transmembrane Protease Serine 2 (TMPRSS2)(Hoffmann *et al.* 2020) on the surface of host cells, promoting the fusion with cell membrane for further release of the genome into the cytoplasm. In the cytoplasm, Open Reading Frames 1a and 1b (ORF1a and ORF1b) are translated from the (+) RNA strand into 16 non-structural proteins, whereas (-) RNA strands are used as template for replication and for the translation of sub-genomic RNAs. Sub-genomic RNAs are then translated into structural proteins, as spike (S), envelope (E), nucleocapsid (N) and membrane (M), that are assembled into viral particles and released to the extracellular space (Finkel *et al.* 2021). During this process, viral RNA may be sensed by innate immunity sensors, as RIG-I(Wu *et al.* 2021) and MDA-5 (Nasirudeen *et al.* 2011; Yin *et al.* 2021) leading to inflammasome activation and cytokine secretion. These interactions trigger signaling pathways that culminate in the production of pro-inflammatory and anti-viral cytokines, as IL-1b, IL-6, TNF- α and type I interferons, which are exacerbated in patients evolving to cytokine storm, as reviewed (Tay *et al.* 2020). Conversely, this is associated with intense lung infiltration of myeloid cells, such as neutrophils (Tay *et al.* 2020; Veras *et al.* 2020) and monocytes, as well as of lymphocytes with high expression of the exhaustion markers, PD-1 and TIM-3(Wauters *et al.* 2021). Clearly, the immune response during COVID-19 has a dual role, as it may reduce viral burden, but also account for disease exacerbation (Gupta *et al.* 2020). These evidences show the complexity of COVID-19 as well as the difficulty in predicting worse disease outcomes.

Accepted Article

In this context, despite being a respiratory disease, COVID-19 patients may develop several other manifestations¹⁸, including anosmia and ageusia (Gerkin *et al.* 2021)¹⁹, suggesting an impact in the central nervous system. In fact, it has been demonstrated that SARS-CoV-2 infects olfactory sensory neurons (OSN) and uses the transmucosal route to reach brain tissue (Meinhardt *et al.* 2021). The neurological importance of SARS-CoV-2 infection is a great matter of debate. A retrospective study performed in Wuhan, China, from January to February 2020 analyzed 214 patients, of whom 36.4% developed neurological symptoms related to cerebrovascular events and impaired consciousness (Mao *et al.* 2020). Since then, many case reports and cohort prospective studies have been published pointing to signs and symptoms of neurological alterations that range from the anosmia and ageusia, to leptomeningitis (Remsik *et al.* 2021), stroke, microvascular damage (Al-Mufti *et al.* 2021), severe headache, encephalopathy (Rehmani *et al.* 2021), and even peripheral Guillain-Barré Syndrome (Fragiel *et al.* 2021). Histopathological analysis revealed multiple ischemic areas, encephalopathy, and microglial activation. Interestingly, recent reports have also pointed to residual psychiatric features in patients that recovered from COVID-19, as chronic fatigue, cognitive decline (Del Brutto *et al.* 2021), mood disorders, depression (Eskandar *et al.* 2021; Nagu *et al.* 2021), during the so-called “brain fog”, long COVID-19 or the Post-Acute Sequelae of COVID-19 (Merad *et al.* 2022) .

Whether these are direct viral effects or indirect results of systemic inflammation is a matter of controversy, and the real impact of SARS-CoV-2 to the human brain remains elusive, and extensively discussed (Awogbindin *et al.* 2021). In this sense, here we used *in vitro* and *in vivo* systems to evaluate brain immunometabolic and energetic changes using Golden Syrian Hamsters (*Mesocricetus auratus*) infected with SARS-CoV-2. We observed that the virus infects hamster’s astrocytes *in vitro* and further inducing a pro-inflammatory response. Interestingly, we observed

that SARS-CoV-2 shifts main metabolic pathways, specially subverting the glutamine usage for enhanced replication. Corroborating this, the blockade of glutaminolysis significantly impairs viral progeny. Also, respirometry confirmed intense metabolic activity in the presence of the virus, further corroborated by metabolomics and metabolites consumption. *In vivo*, we confirmed the presence of viral RNA in the cortex and hippocampus of infected animals, associated with consistent changes in the protein profile. Thus, here we suggest that the virus hijacks cellular carbon metabolism, especially glutamine consumption, for its own benefit, in detriment of a proper cellular metabolic function. Due to the importance of glutamatergic transmission for appropriate neuronal synaptic formation and connectivity, here we propose a correlation between SARS-CoV-2 infection over memory and cognition due to metabolic imbalance of important neurotransmitters, especially glutamate/glutamine. Moreover, our proteomic analysis showed a significant impact on carbon metabolism pathways consistent with brain diseases, such as Parkinson's Disease, Multiple Sclerosis, and long-term depression, which were also concordant with changes observe in COVID-19 deceased patients. This brings attention to a possible correlation of altered carbon and energy metabolism with the cognitive and memory impairment observed in patients with long COVID-19 or PASC.

MATERIALS AND METHODS

This study was not pre-registered.

Virus isolation and propagation

SARS-CoV-2/SPPU-0691 (GenBank accession number MW441768) was obtained, isolated, and propagated at Scientific-Platform Pasteur-USP (SPPU) and used for the experiments *in vitro*. The respiratory sample (naso-oro-pharyngeal swab) was acquired during the acute phase of infection

Accepted Article

and complying with the inclusion criteria for clinical suspicion of associated viral infection to SARS-CoV-2 adopted by the Ministry of Health of Brazil. Viral stocks were generated in Vero CCL81 cells (RRID CVCL_0059). Prior to infection, cells were maintained in DMEM Low glucose (LGC[®]) supplemented with 10% of fetal bovine serum (FBS) (Gibco[®]) and 1% penicillin/streptomycin (LGC[®]) at 37°C, 5% CO₂. The initial inoculum (passage 1) was prepared to dilute the clinical samples (1:5) in non-supplemented DMEM low glucose (Gibco[®]). The inoculum was then added to the flask containing Vero cells and maintained for 1 hour at 37°C, following addition of fresh DMEM low glucose media supplemented with 2% FBS and 1% penicillin/streptomycin. The cell culture was observed for cytopathic effects on each day after the inoculation. When a prominent cytopathic effect was observed the cell culture supernatant was collected, centrifuged to remove debris (500g), and stored at -80°C as the first viral passage. The same strategy was employed three times to obtain a fourth passage isolate. Fourth passage viral stocks were used in this study titrated by plaque-forming unit (PFU) assay, according to protocols described elsewhere (Araujo *et al.* 2020). SARS-CoV-2 strain human/BRA/SP02cc/2020 (GenBank access number: MT350282.1) was used in the *in vivo* experiments.

Primary astrocytes cultures of Golden Syrian Hamsters (*Mesocricetus auratus*)

Primary astrocytes were obtained from Syrian hamster neonates at days 2-4 postpartum (dpp). The protocols were approved by the Ethics Committee for Animal Research of University of Sao Paulo (CEUA n° 7971160320 / 3147240820) and all efforts were made to minimize animal suffering. Animals were obtained from the Department of Pathology, School of Veterinary Medicine and from the Animal Science Department of Preventive Veterinary Medicine and Animal Health from the University of São Paulo. Briefly, brains were harvested, and the meninges were removed following tissue digestion with 0.05% of trypsin (Gibco[®]) at 37°C for 10 minutes. Next, tissue was

mechanically disrupted and centrifuged 500g for 5 minutes. Cells were then resuspended in DMEM Ham's-F12 (LGC[®]) supplemented with 10% FBS (Gibco[®]), 1% penicillin/streptomycin, 1% non-essential amino acids (NEEA) (LGC[®]), 1% sodium pyruvate (LGC[®]) and 1% L-glutamine (LGC[®]) and seeded in culture flasks maintained overnight at 37°C, 5% CO₂ atmosphere. Cells were then washed with phosphate saline buffer (PBS) and replaced with fresh media. The media were changed every three days until the confluency was reached, when culture flasks were shaken at 200rpm for 3 hours at 37°C for detaching of microglia. Floating cells were removed, and the remaining attached cells were harvested for *in vitro* assays.

***In vitro* infection with SARS-CoV2**

Primary astrocytes were infected with SARS-CoV-2 at MOI 0.1 for 1h at 37°C and 5% CO₂ atmosphere. After infection, inoculum was washed, and cells were incubated with fresh DMEM HAMs F-12 supplemented with 10% FBS (LGC[®]), 1% penicillin/streptomycin (LGC[®]), 1% NEAA (LGC[®]), sodium pyruvate (LGC[®]) and L-glutamine (LGC[®]) at 37°C and 5% CO₂ atmosphere. Supernatant and cells were harvested after 24-, 48- or 72-hours post infection for further analysis. For the experiments with inhibitors, astrocytes were treated with inhibitors for 2h prior to infection. For experiments with glucose (17 mM) and glutamine (2mM) supplementation, supplementation was also added 2h prior infection.

***In vivo* Infection of Golden Syrian Hamsters with SARS-CoV-2**

SARS-CoV-2 strain human/BRA/SP02cc/2020 (GenBank access number: MT350282.1) was used in the *in vivo* experiments of this study. This virus was obtained from nasopharyngeal swabs from the first patient (HIAE01) to be diagnosed with COVID-19 in Brazil (Araujo *et al.* 2020), isolated in Vero ATCC CCL-81 cells and quantified by using the Median Tissue Culture Infectious Dose

(TCID₅₀) assay. This sample was also confirmed to be free of other common 18 human respiratory viruses using a qPCR respiratory panel. A third passage aliquot was used to infect the hamsters. Brain samples from SARS-CoV-2-infected and uninfected hamsters from two unrelated experiments were used herein (one performed with 15–16-week-old females and another with 18-week-old males). Accordingly, conventional hamsters were acquired from the Gonçalo Muniz Institute, Fiocruz, Salvador, Brazil and maintained at the biosafety level 3 animal facility of the Department of Parasitology, Institute of Biomedical Sciences (ICB), USP, Brazil, with food and water ad libitum. Animals were housed in pairs and groups homogenized based on weight. Animal procedures were approved by the Institutional Animal Care and Use Committees of the ICB and the College of Veterinary Medicine, USP (protocols #9498230321, #3147240820, #2076201020). In both experiments, animals were anesthetized intraperitoneally with 100 mg/kg of ketamine and 5 mg/kg of xylazine at day zero for the intranasal inoculation of 50 µl of 1×10^5 TCID₅₀ of SARS-CoV-2 suspended in DMEM with 2% FBS (infected group) or 50 µl of sterile DMEM with 2% FBS (uninfected, mock group). Hamsters were followed daily for clinical signs and weight. Subgroups (n = 3 to 5) of animals were euthanized with a combination of 5 mg/kg of morphine followed by an overdose of ketamine (600mg/kg) and xylazine (30 mg/kg) on days 3, 4, 5, 7 and/or 14 post-infection, depending on the experiment. Brains were collected aseptically at necropsy, using sterile surgical forceps and scissors, and directly placed in 50 mL falcon tubes with DMEM. Brain samples were collected from three infected female hamsters on day 3, and five infected and four uninfected hamsters on day 7. Brain samples were collected from 5 infected male animals on days 3, 5, 7, and 14, and from three non-infected hamsters on day 7.

Drugs and Inhibitors

This study was conducted using the following drugs and inhibitors: 6-diazo-5-oxo-L-nor-Leucine, 50uM (DON, Cat. Number. 157-03-9; Cayman Chemicals, Ann Arbor, Michigan, USA); 2-deoxy-D-Glucose-6-phosphate, 5mM (2-DG, Cat. Number.17149; Cayman Chemicals, Ann Arbor, Michigan, USA) and Etomoxir, 3uM (Cat. Number. 11969; Cayman Chemicals, Ann Arbor, Michigan, USA).

Cytotoxicity assay

Cytotoxicity of each metabolic pathway inhibitor was performed with alamarBlue™ reagent according manufacturer guidelines. Briefly, primary Syrian hamster's astrocytes were plated in 96-well plate and treated with 2-DG (range of 0.05 to 500mM), Etomoxir (range of 0.03 to 300µM) or DON (range of 0.05 to 500 µM) for 72 hours (the same time point used in all experiments) before the addition of alamarBlue™ diluted 1:10. Cells were incubated with alamarBlue™ for 4 hours and analyzed by plate reader at wavelengths of 570nm and 600nm. Survival was calculated according to reduction percentage relative to untreated cells.

Plaque-forming unit assay

For virus titration, Vero CCL81 cells were seeded in 24 well plates one day before the infection for adhesion. Supernatants from *in vitro* assays were serially diluted in pure DMEM low glucose and inoculated for 1 hour at 37°C. Next, the inoculum was removed and replaced with DMEM low glucose containing 2% FBS, 1% penicillin/streptomycin and 1% carboxymethylcellulose. After 3 days, the media was removed, and the cells fixed with 3.7% formaldehyde overnight. The cell monolayers were stained with 1% crystal violet for 15 minutes. The viral titer was calculated based on the count of plaques formed in the wells corresponding to each dilution expressed as plaque-forming units per mL (PFU/mL).

RNA extraction, viral load, and gene expression analyses

RNA extraction from cell lysates was performed using the MagMAX™ Viral/Pathogen II (MVP II) Nucleic Acid Isolation Kit (Catalog number: A48383) (Applied Biosystems®) and carried out according to the manufacturer's instructions. RNA extraction was performed using Trizol® reagent (ThermoFisher®) and carried out according to the manufacturer's instructions. RNA quantity was determined by NanoDrop (ThermoFisher®). Total RNA samples (up to 2 µg) were reverse transcribed using the oligo(dT) primer from the High-Capacity cDNA Reverse Transcription Kit (Thermo Fisher®). Molecular detection of SARS-CoV-2 was performed with TaqMan™ Gene Expression Assay (Cat. N. 4331182, ThermoFisher®) with specific primers/probes previously described⁴⁰. The quantitative assay was performed using a standard curve produced with serial dilutions of SARS-CoV-2 RNA expressed on a Briggsian logarithm scale as genome equivalents per µg of total RNA. Gene expression assays were performed using Power SYBR® Green Master Mix (Cat. N. 4368577, ThermoFisher®) with primers described below. For the subgenomic RNA (sgRNA) detection, we utilized a combination of the Envelope primer and probe in combination of the sgRNA primer as described elsewhere (Wölfel *et al.* 2020). The median cycle threshold (C_t) value from experimental replicates and 2^{-DDC_t} method were used for relative quantification analysis and all C_t values were normalized to *Actb*. All qRT-PCR assays were performed on QuantStudio™ 3 Real-Time PCR System (Thermo Fisher®).

Table 1. Primers used for gene expression analysis

Target gene	Primer sequence (5'- 3')
<i>Actb</i> _Hm	F – AAGATGACCCAGATCATGTTTGAG R - ACGTACATGGCTGGGGTGTG
SARS-CoV-2 (E_Sarbeco)	F - ACAGGTACGTTAATAGTTAATAGCGT

	R - ATATTGCAGCAGTACGCACACA P1 FAM - AACTAGCCATCCTTACTGCGCTTCG-BHQ1
SARS-CoV-2 (sgRNA)	F - ACAGGTACGTTAATAGTTAATAGCGT R - CGATCTCTTGTAGATCTGTTCTC P1 FAM - AACTAGCCATCCTTACTGCGCTTCG-BHQ1
<i>Ifitm3_Hm</i>	F - AGCAGCCTTTTCTTGACAGC R - ACCATTCCGCAACACACTTC
<i>Il-6_Hm</i>	F - GGACAATGACTATGTGTTGTTAGAA R - AGGCAAATTTCCCAATTGTATCCAG
<i>Ace-2_Hm</i>	F - TCTCAGCCTTGTTGCTGTTGCT R - AGACAGGTCTTCAGCTTCCTGGT
<i>Tnfa_Hm</i>	F - TGAGCCATCGTGCCAATG R - AGCCCGTCTGCTGGTATCAC
<i>Isg20_Hm</i>	F - TGCAGCATTGTGAACTTCAGTG R - GCAGGATCTCTAGTCTGGCTTC
<i>Il-1b_Hm</i>	F - TTCTGTGACTCCTGGGATGGT R - GTTGGTTTATGTTCTGTCCGTTG
<i>Ifna_Hu</i>	F - CTGGTGGCTGTGAGGAAATA R - AGCAAGTTGGCTGAGGAAGA
<i>Slc1a3</i>	F - CTGGGGAAGGCAAACAGAAGA R - TGGGAGGGATGAGGAAAAGTG
<i>Slc1a2</i>	F - ATCCAGCCCTGACCACAATG R - TAGCGGAGGCAAGAGTTTGG
<i>Grin2a</i>	F - CACGTCCAGCAAGGGAGATT R - CTACCCTCGGTGTTGTGCAT
<i>Grin2b</i>	F - GGGGCTTTGGAACGGAGTAA R - AACAGCATACGGTGGCTTCA

Proteomics

LC-MS/MS Analysis

After infection hamster astrocytes were resuspended in lysis buffer (100mM Tris HCL, 150 mM NaCl, 1 mM EDTA, 1% Triton X) with freshly added protease and phosphatase inhibitors

(Protease Inhibitor Cocktail, SIGMA®) and subjected to ultrasonication (3 cycles of 20s). Samples were submitted to the FASP protocol (Distler U., and Tenzer S., 2016). Samples had their buffer exchanged in a microcolumn tip with a 10kDa MW cut off. Tryptic digestion was performed in column. Forty micrograms of protein were used to carry out the FASP protocol, where the samples were reduced, alkylated, and later digested using trypsin. Digested peptides from each sample were resuspended in 0.1% formaldehyde. The separation of tryptic peptides was performed on an ACQUITY MClass System (Waters Corporation®). One µg of each digested sample was loaded onto a Symmetry C18 5 µm, 180 µm × 20 mm precolumn (Waters Corp®) used as trapping column and subsequently separated by a 120 min reversed phase gradient at 300 nL/min (linear gradient, 3–55% ACN over 90 min) using a HSS T3 C18 1.8 µm, 75 µm × 150 mm nanoscale and LC column (Waters Corp®) maintained at 30 °C. For the gradient elution water-Formic Acid (99.9/0.1, v/v) has been used as eluent A and Acetonitrile Formic Acid (99.9/0.1, v/v) as eluent B. The separated peptides were analyzed by High Definition Synapt G2-Si Mass spectrometer directly coupled to the chromatographic system. Differential protein expression was evaluated with a data-independent acquisition (DIA) of shotgun proteomics analysis by Expression configuration mode (MSe). The mass spectrometer operated in “Expression Mode” switching between low (4 eV) and high (25–60 eV) collision energies on the gas cell, using a scan time of 1.0s per function over 50–2000 m/z. All spectra were acquired in Ion Mobility Mode by applying a wave velocity for the ion separation of 1.000m/s and a transfer wave velocity of 175m/s. The processing of low and elevated energy, added to the data of the reference lock mass ([Glu1]-Fibrinopeptide B Standard, Waters Corp®) provides a time-aligned inventory of accurate mass retention time components for both the low and elevated-energy (EMRT, exact mass retention time). Each sample was run in three technical replicates. Continuum LC-MS data from three replicate experiments for each sample

Accepted Article

have been processed for qualitative and quantitative analysis using the software Progenesis (Waters Corp[®]). The qualitative identification of proteins was obtained by searching in an unreviewed database *Mesocricetus auratus* (Syrian Golden hamster) UNIPROT Proteome ID UP000189706. Search parameters were set as: automatic tolerance for precursor ions and for product ions, minimum 1 fragment ions matched per peptide, minimum 3 fragment ions matched per protein, minimum 1 unique peptide matched per protein, 2 missed cleavage, carbamidomethylation of cysteines as fixed modification and oxidation of methionine as variable modifications, false discovery rate (FDR) of the identification algorithm < 1%. Label free quantitative analysis was obtained using the relative abundance intensity integrated in Progenesis software, using all peptides identified for normalization. The expression analysis was performed considering technical replicates available for each experimental condition following the hypothesis that each group is an independent variable. The protein identifications were based on the detection of more than two fragment ions per peptide, and more than two peptides measured per protein. The list of normalized proteins was screened according to the following criteria: protein identified in at least 70% of the runs from the same sample and only modulated proteins with a $p < 0.05$ were considered significant.

Metabolomics of Hamsters astrocytes

Hamster's primary astrocytes were cultured as described above. Next, the medium was washed twice with phosphate-buffered saline (PBS) at physiologic pH and cells were collected with 600 μ L of methanol (MeOH). Finally, the samples were dried and stored in the freezer at -80 °C until metabolites extraction.

Bligh-Dyer polar metabolites extraction: Volumes of 150 μL of water (H_2O), 190 μL of methanol (MeOH), and 370 μL of chloroform (HCCl_3) were added, and then the tubes were shaken vigorously for 2 minutes. Subsequently, the dimensions were centrifuged for 5 minutes at 13,000 g. The aqueous supernatant was collected and dried for 60 in a concentrator. All samples were stored in a freezer at -80°C until analyzed by UPLC-MS/MS.

Metabolites Analysis: The samples were resuspended in 80 μL of a 1:1 mixture of acetonitrile:water ($\text{ACN}:\text{H}_2\text{O}$). For each analysis, we injected 3 μL of sample, and the separation was performed by hydrophobic interaction liquid chromatography (HILIC) analysis using an acquity UPLC[®] BEH amide 1.7 mm, 2.1 mm x 100 mm column. The mobile phases used for the separations were $\text{ACN}:\text{H}_2\text{O}$ (80:20) as mobile phase A and $\text{ACN}:\text{H}_2\text{O}$ (30:70) as mobile phase B, containing 10 mM of ammonium acetate ($\text{NH}_4\text{CH}_3\text{COO}$) and 0.1% of ammonium hydroxide (NH_4OH) was additive in both mobile phases. Then, the separation was performed by isocratic flow of 0.3 mL/min, to start with 99% A and was up to 1% A in 7 min. In the final part, we return to 99% A in 1 min and remain for 2 min to equilibrate the column before the next injection. The total run time was 10 min. Negative ion mode was recorded and the instrument was operated in MS E mode in the m/z range of 50–800 Da, with an acquisition time of 0.1 s per scan. The raw files were preprocessed by Progenesis QI Waters[®] software. The identification was performed with a 5-ppm error for the precursor ion.

Real-time metabolic assays

An XFe24 Extracellular Flux analyzer (Agilent[®]) was used to determine the bioenergetic profile. Cells were plated at 2×10^4 cells per well in XFe24 plates 24h before infection with SARS-CoV-2. Glycolytic Stress and Mito Stress Tests were performed on XFe24 Bioanalyzer at 72 hpi. All

assays were performed following manufacturer's protocols. Results were normalized to cell number.

Electron microscopy

Hamster astrocytes infected and uninfected were recovered, washed with PBS 1x, and fixed with Glutaraldehyde 4% overnight. Samples were washed with PBS 1x and followed to dehydration process with acetone gradient, desiccation, and gold metallization. Finally, samples were analyzed in JOEL1010 transmission electron microscope. Generated images were loaded into Fiji software for further analysis. For TEM mitochondrial measurements, the images were filtered and manually measured for width and length.

Mitochondrial analysis

For measurements of mitochondrial superoxide, the cells were stained with LIVE/DEAD™ Fixable Green (L34970; ThermoFisher®, 15 min) and MitoSOX™ Red mitochondrial superoxide indicator (M36008; ThermoFisher®; 2.5uM, 10 min). Cells were then washed with warm 1X PBS and fixed with 4% PFA for 15 minutes at 4C. Next, cells were analyzed using a Accuri C6 Plus (BD Biosciences®) cytometer and data analyzed using FlowJo X software.

Immunofluorescence

On day 7 of astrocyte culture, 2×10^4 cell were seeded in a 24-well plate, after overnight incubation with culture media cells were fixed with ice-cold 4% paraformaldehyde in 0.1 M phosphate buffer pH 7.4 for 30 minutes. After antigen retrieval (Tris/EDTA-Tween-20 buffer - 10mM Tris, 1mM

Accepted Article

EDTA, 0.05% Tween 20, pH 9 - for 30 minutes at 95°C, followed by 20 minutes at room temperature), cells were permeabilized with 0.5% Triton-X100 in PBS for 10 minutes, blocked with blocking solution (5% donkey serum + 0.05% Triton X-100 in PBS) (Sigma-Aldrich) for 2 hours at room temperature and incubated with primary antibodies: Serum produced in rat anti-spike fragments 420,561 e 741 (1:100), kindly provided by Prof. Edison Luiz Durigon, ICB-USP; GFAP (1:1000, Sigma-Aldrich, Cat. Number: G9269), IBA1 (1:500, Abcam Cat. number: ab5076), and MAP2 (1:500, Sigma-Aldrich Cat. number: M3696) diluted in blocking solution, overnight at 4°C. The cells were PBS washed and incubated with secondary antibodies (AlexaFluor 594; AlexaFluor 488; 1:2000, Invitrogen) diluted in PBS + 0.05% Triton X-100 for 2 hours at room temperature, protected from light. For nuclear staining, cells were incubated for 20 minutes at room temperature with DAPI (4',6'-diamidino-2-phenylindole; 1:150000, Sigma-Aldrich), mounted on glass slides with Fluoromount-G (Invitrogen) mounting medium and sealed with nail polish. Images were acquired using Nikon Eclipse 80i fluorescence microscope (Nikon Instruments Inc., NY, USA) coupled with Nikon Digital Camera DXM 1200 C. Quantification was made using ImageJ software (NIH), where 5 to 10 randomly chosen visual fields per coverslip from three independent cultures were analyzed.

Hamster brain slice culture and SARS-CoV-2 infection.

Brain sections were obtained from male hamsters and prepared as previously described, with modifications (Fernandes *et al.* 2019; Mendes *et al.* 2018). Whole brain - cerebellum and brainstem were removed - was sliced at 200 µm in a VT1000s automatic vibratome (Leica) and cultivated free-floating with Neurobasal A (Gibco) medium supplemented with 1% Glutamax (Gibco), 1% penicillin/streptomycin (Gibco), 2% B27 (Gibco), and 0.25µg/mL fungizone (Sigma). For virus infection, the medium was removed, and the brain slices were exposed to 3x10⁶ TCID₅₀ of SARS-

CoV-2 or an equivalent volume of mock medium. Infection was performed for 2h at 37°C and 5% CO₂ in a biosafety level 3 laboratory. The inoculum was removed, the tissue was washed, and the slices were maintained in fresh medium at 37°C and 5% CO₂ until processing for subsequent analysis. This procedure was approved by the CEUA-FMRP (#066/2020).

Single Nuclei Transcriptomic Profile Analysis

Raw snRNA-seq data were obtained from frozen medial frontal cortex tissue from six post-mortem control and seven COVID-19 patients assessed herein were obtained from the dataset GSE159812 on NCBI GeneExpression Omnibus public databank. Reads were aligned to the hg38 genome (refdata-gex-GRCh38-2020-A) using Cell Ranger software (v.6.0.0) (10x Genomics) generating the raw gene counts matrix. Reads mapping to pre-mRNA were also counted to account for unspliced nuclear transcripts. After quantification using the Cell Ranger count pipeline on each individual library, the Cell Ranger aggr pipeline was used to aggregate the libraries into two distinct groups, control and infected. We subsequently used these grouped matrices as input to downstream analysis in Seurat (version 4.0.4)(Hao *et al.* 2021), initially filtering nuclei with unique molecular identifiers over 2,500 or less than 200, besides outliers with more than 5% mitochondrial counts. We performed normalization regressing out heterogeneity associated with mitochondrial contamination fitting the counts to a Gamma-Poisson General Linear Model, removing this confounding source of variation through scTransform Seurat's function (Hafemeister and Satija 2019) and glmGamPoi package (Ahlmann-Eltze and Huber 2020). Integration of both groups was executed identifying cross-dataset pairs of cells that are in a matched biological state ('anchors'), correcting technical differences between those groups to improve comparative snRNA-seq analysis. Dimensionality reduction was implemented by Principal Component Analysis, followed

by UMAP embedding using the first 20 principal components, the same parameter as used for clustering with both FindNeighbors and FindClusters (at 0.5 resolution) Seurat's functions. Marker genes were identified through MAST positive differential expression (Finak *et al.* 2015) of each cluster against all others and cell types annotation was achieved using previously published marker genes (Jiang *et al.* 2020). Differential gene-expression comparison between the control individuals and infected patients was done using the MAST algorithm (v.1.18.0). Genes with fold change > 0.25 (absolute value), adjusted p value (Bonferroni correction) < 0.1 and detected in a minimum fraction of 10% nuclei in either of the two populations were considered differentially expressed. Differentially Expressed Genes (DEGs) corresponding to the Differentially Expressed Proteins (DEPs) from hamster brain proteomics and concordant fold-change were subjected to Gene Ontology analysis, performed through online database PANTHER using PANTHER Pathways dataset (Mi *et al.* 2019).

Statistical analysis

No randomization was performed to allocate subjects in the study. No blinding experimentation nor analysis was performed. No test for outliers was conducted thus. Data was plotted and analyzed using the GraphPad Prism 8.0 software (GraphPad Software[®], San Diego, CA). For analyses between 2 groups, Student's *t* test two-tailed was used and p-value, t-value, and degrees of freedom (DF) are found in figure's legends. For comparisons among 3 or more groups, *One-way* ANOVA, followed by adequate post hoc tests was used as described in figures legends. p-value, F and DF are also found in figure's legends. Differences were considered statistically significant when p value was <0.05.

RESULTS

SARS-CoV-2 infects Syrian hamsters' astrocytes

We started our experiments by infecting brain slices of adult Syrian golden hamsters with 3×10^6 TCID₅₀ of SARS-CoV-2 (Supplementary figure 1A). Tissue infection was confirmed by spike protein detection in GFAP⁺ astrocytes (Supplementary figure 1B) and corroborated by increased nucleocapsid RNA (N1) concentration 48 hpi (Supplementary Figure 1C). Thus, we decided to specifically investigate the impact of SARS-CoV-2 infection on astrocytes. For that, hamster's primary cultures obtained from 2-4 days old pups composed of more than 80% astrocytes and very few neurons and microglia (Supplementary Figure 2A-D) were infected with MOI 0.1 of SARS-CoV-2 (strain SPPU-0691/B.1.1.28 Genbank: MW441768#). Confirming data from tissue slices, we detected SPIKE proteins in GFAP⁺ cells (Figure 1A-C). Conversely, increased amounts of SARS-CoV-2 RNA were detected in the cell cultures at 48- and 72-hours post infection (hpi) (Figure 1B) confirmed by viral particles detected in the culture supernatant in which the viral load was significantly increased at 72 hpi compared to 24 hpi for both MOIs tested (Figure 1C). Next, we performed qPCR for genomic and subgenomic amplification to confirm viral replication. As shown in Figure 1F, there was a positive correlation at 24, 48 and 72 hpi ($R=0,9$; $p=0,083$). We also performed transmission electron microscopy (TEM) for viral particles visualization. Figure 1D shows viral particles attached to the cell surface (black arrowheads), as well as the presence of double-membrane vesicles (asterisks), characteristics of coronavirus infection (Eymieux *et al.* 2021).

SARS-CoV-2 astrocyte infection induces pro-inflammatory cytokines, interferon-stimulated genes and changes the expression of carbon metabolism related proteins *in vitro*

Next, we evaluated whether SARS-CoV-2 changes the overall expression of proteins and the production of pro-inflammatory cytokines in hamster's primary astrocytes. As shown in Figure 2A, principal component analysis (PCA) of proteomics evidences the differential clusterization of control vs. infected samples at 72 hpi. Next, and consistent with the literature, we observed that *Il-1b*, *Il-6*, *Tnf-a* and *Ifn-a* are significantly increased 72 hpi at MOI 0.1 (Figure 2B-E). Confirming that type I interferons are active, we also observed that the interferon-stimulated genes (ISGs), *Isg20*, *Iftm3* and including *Ace-2*, were up-regulated (Figure 2 E-H).

Through proteomic analysis we observed the differential expression of 646 proteins (DEP), of which 568 were up-regulated and 78 down-regulated in infected cells compared to controls (10 controls vs 8 SARS-CoV-2) (Figure 2I and Supplementary Figure 3A). A pathway-protein analysis using Kyoto Encyclopedia of Genes and Genomes (KEGG) database evidenced that the great majority of DEP were correlated to carbon metabolism (Got1, Eno3, Aldoc, Tald1, Pgk1, Ogdh, Pkfp, Pfk1, Gfpt), tricarboxylic acid cycle (Mdh1, Acly, Sdha, Ogdh, Dlst, Idh1, Cs, Suclg1), glycolysis (Aldoc, Gapdhs, Pgk1, Ldhd, Pfk1, Eno3, Pfkp, Eno1, Pgk2, Pklr, Aldh9a1), as well as to protein processing in the endoplasmic reticulum (Pdia3, Cryab, Dnajb11, Sec23a, Lman1, Hsph1) (Figure 2J and Supplementary Figure 3B). Of note, these proteins are enriched in pathways that are also dysregulated in several brain diseases, such as Huntington Disease (HD), Parkinson's Disease and Amyotrophic Lateral Sclerosis (ALS) (Nefh, Rab1a, Rab39b, Pfn1, Psma4, Psmc6, Ndufv2, Gnai3, Ap2a1, Slc25a5) (Figure 2J and Supplementary Figure 2B). Conversely, by comparing our data with data sets from human brain samples from SARS-CoV-2 infected subjects, we observed an overlap of approximately 53 proteins (Supplementary Figure 3C). Consistently, most of these changes are related to alterations in the overall metabolic profile of the cells,

including carbon metabolism, glycolysis/gluconeogenesis, and pentose phosphate pathway (Supplementary Figure 3D).

SARS-CoV-2 induces metabolic changes in astrocytes *in vitro*

Because SARS-CoV-2 infection induced important changes in carbon metabolism-related proteins, we next validated these findings. First, we infected the cultures with SARS-CoV-2 (MOI 0.1) and assessed mitochondrial morphology through transmission electron microscopy (TEM). As shown in Figure 3A, mitochondria from SARS-CoV-2 samples are more fragmented than in control cultures. This was associated with increased mitochondrial reactive oxygen species (ROS) production at 24 and 72 hpi (Figure 3B). Next, we performed high resolution real-time respirometry at 72 hpi. Conversely, we observed that both glycolytic and non-glycolytic acidification were increased in the presence of the virus (Figure 3C – Supplementary Figure 4), although, basal and maximal mitochondrial respiration were not statistically different, despite the trend (Figure 3D).

SARS-CoV-2 changes the metabolic profile of hamsters' primary astrocytes

To deeply characterize the metabolic changes induced by SARS-CoV-2 infection in astrocytes, we performed a targeted metabolomic analysis at 72 hpi with MOI 0.1. We observed a significant reduction in almost all metabolites evaluated (Figure 4). Glucose was reduced (Figure 4A) as well as many of the TCA cycle precursors, such as lactate (Figure 4B), pyruvate (Figure 4C), serine (Figure 4D), acetate (Figure 4E), aspartate (Figure 4J) 2-hydroxyglutarate (Figure 4M) as well as succinate (Figure 4L), strongly suggesting anaplerotic reactions to supply the synthesis of biomolecules, which may be involving in supporting viral replication. Interestingly, although glutamate levels were maintained, there was a significant decrease of glutamine (Figure 4G),

alpha-ketoglutarate (Figure 4K) and 2-hydroxyglutarate (Figure 4M) levels in infected samples. The levels of GABA (Figure 4I), another glutamate precursor, was unchanged. Interestingly, palmitate levels were increased (Figure 4F), further suggesting that TCA intermediates are being used as building blocks for other biomolecules, such as lipids. Altogether, our data show an intense activation of cataplerotic and anaplerotic pathways, especially with a switch to glutamine and alpha-ketoglutarate consumption and lipid synthesis.

SARS-CoV-2 replication in astrocytes is dependent on glutamine

To further determine which specific metabolic pathway is more important in favoring SARS-CoV-2 replication, we treated infected cultures with inhibitors of fatty acid metabolism (Etomoxir), glutaminolysis (L-DON) and glycolytic pathways (2-DG) (Figure 5A). As illustrated in Figure 5B, we first evaluated cell viability in the absence of infection to select the correct drug concentration and to avoid bias of cell death during the experiments. Further, as illustrated by Figure 5C, blockade of glycolysis with 2-DG did not significantly change SARS-CoV-2 replication at 24-72 hpi, further corroborated by PFU assay (Figure 5C). Also, the use of etomoxir, an inhibitor of the carnitine palmitoyltransferase 1a (CPT-1a), indicates low dependence of mitochondrial fatty acid oxidation (Figure 5C-D). Interestingly, the inhibition of mitochondrial glutaminase (GLS) with L-6-Diazo-5-oxo-norleucine (L-DON), did not change genome replication (Figure 5C), but significantly decreased the release of viral particles (Figure 5D). Accordingly, the addition of glutamine (2mM) in the absence of glucose significantly increased viral replication, whereas glucose (17mM) was not able to do so (Figure 5E).

Next, we evaluated the expression of proinflammatory cytokines during the treatment with L-DON. Blockade of GLS with L-DON decreased the transcription of *Il-1b*, *Il-6* (Figure 5F-G),

and *Ifn-a* (Figure 5I) but not *Tnf-a* (Figure 5H) when compared to non-treated groups. This is in accordance with the reduction of the ISGs, *Ace-2*, *Isg20* and *Iftm3* (Figure 5J-L). These results evidence that glutamine is important for viral replication and the blockade of glutaminolysis reduces viral loads which in turn reduces type I IFN and pro-inflammatory responses.

SARS-CoV-2 RNA is detected in the cortex, hippocampus, and olfactory bulb of hamsters *in vivo*.

It has already been demonstrated that the Syrian hamster is a permissive model to nasal infection with SARS-CoV-2 (Imai *et al.* 2020). Thus, we decided to use this model to address whether the virus reaches important areas of the brain, such as cortex, hippocampus, and olfactory bulb after intranasal infection with 10^5 TCID₅₀, as illustrated. Consistently, we confirmed the presence of SARS-CoV-2 in these areas, both at 3-, 5-, 7- and 14-days post-infection (dpi) (Figure 6A) with higher titers at day 3. To confirm genome replication, we performed qPCR for genomic and subgenomic fractions. As observed *in vitro*, there was a positive correlation in the hippocampus (R=0,062; p=0,011), cortex (R=0,758; p=0,025), olfactory bulb (R= 0,771; p=0,0019) and other areas (R= 0,74; p=0,00067). We also observed increased expression of the same pro-inflammatory cytokines evaluated *in vitro*, as *Il-6*, *Il-1b* and *Tnfa*, as well as the ISGs *Isg20* and *Iftm3*, both in the hippocampus (Figure 6B) and cortex (Figure 6D). Interestingly, although *Il-1b* was increased in the cortex (Figure 6D), no difference was observed in the hippocampus (Figure 6B). The same was observed for *Il-6* which is increased the hippocampus (Figure 6B) but not in the cortex (Figure 6D). As expected, proteomic analysis of these brain samples showed that in the hippocampus, DEPs correlated with pathways of oxidative

phosphorylation, long-term potentiation, dopaminergic and cholinergic synapses, among others (Figure 6C). In the cortex, DEPs correlated with important neuronal function, as synaptic vesicle cycle, dopaminergic and GABAergic synapses, as well as to neurological features of brain diseases, as Parkinson's disease and long-term depression (Figure 6E). To further confirm whether these changes are in accordance with those observed in human COVID-19 patients, we compared the DEPs from our *in vivo* proteomic analysis with a data set from the literature that analyzed more than 64,000 single cells obtained from the frontal cortex and choroid plexus of 8 deceased COVID-19 patients (Figure 6F). We found a strong convergence of important signaling pathways enriched in both datasets, such as those for metabotropic and ionotropic glutamate receptors, Wnt signalling and adrenergic activation. Also, important physiological processes were related between hamster and human samples, as synaptic vesicle trafficking, glycolysis, and inflammation, which were further consistent with the enrichment of DEPs correlated to brain diseases, as Parkinson's disease, Huntington's disease, and Alzheimer's disease (Figure 6G). We also performed qPCR for the expression of glutamate transporters and receptors in the hippocampus and cortex of the infected animals, but we detected no differences (Supplementary Figure 5 B-C)). Next, we also compared our proteomics with single cell specific populations from the human brains, as astrocytes, microglia and excitatory neurons (Supplementary Figure 6). Altogether, our data support the hypothesis that important changes in protein expression and carbon metabolism are occurring in the brains of infected Golden Syrian hamsters, and these changes may share similarities to those observed in COVID-19 patients.

DISCUSSION

Although the great majority of people infected with SARS-CoV-2 develop only mild or asymptomatic disease, COVID-19 has already taken more than 6.2 million lives worldwide.

Moreover, although it is essentially a lung disease, unconventional neurological symptoms have been reported since the beginning of the pandemic: from mild anosmia and ageusia, to more severe neurological cases of encephalitis, cerebrovascular disease, ataxia and seizures (Wang *et al.* 2021). Most recently, the description of the long COVID-19, "brain fog" or the PASC (Merad *et al.* 2022; Whitaker *et al.* 2022) still intrigues physicians and researchers, as cases of cognitive impairment, memory decline, disorientation, chronic fatigue and depression have been increasing significantly (Whitaker *et al.* 2022), evidencing the complexity of the disease (Piras *et al.* 2014; Merad *et al.* 2022).

In this context, here we show that SARS-CoV-2 infects the central nervous system of Syrian hamsters, *Mesocricetus auratus*, *in vitro* and *in vivo*. More importantly, we observed that the infection actively changes both metabolic and proteomic profile of astrocytes *in vitro* and whole tissue, *in vivo*. Proteomic analysis of primary astrocytes *in vitro*, as well as dissected cortex and hippocampus *in vivo*, demonstrated relevant changes in proteins related to carbon metabolism, biosynthesis of amino acids and the tricarboxylic acid cycle (TCA) This was further corroborated by the overall increase in glycolysis and oxygen consumption assessed by respirometry, which has already been demonstrated in mononuclear and lung cells (Codo *et al.* 2020; Krishnan *et al.* 2021). Conversely, KEEG pathway analysis evidenced a conversion to pathways enriched in neurological diseases such as Huntington disease, Parkinson disease and long-term depression, whose several symptoms are similar to those observed in PASC patients.

The fact that viruses actively hijack cellular metabolism is well known, as for CMV, HSV, HIV, vaccinia virus (Fontaine *et al.* 2014), and many others, as reviewed (Bharadwaj *et al.* 2021). This occurs either to facilitate viral replication and virion assembling or to evade local immune responses. Thus, due to the complexity and the refined metabolic necessities of brain cells for

proper brain function, it is reasonable to believe that SARS-CoV-2 impacts brain function through metabolic or neurochemical imbalance. Moreover, it is becoming clearer that the virus is capable of reaching and replicating in brain tissue of both mouse (Song *et al.* 2021b) and humans (Song *et al.* 2021a; Crunfli *et al.* 2020), and its impact on neurological function has become unquestionable. In fact, it has been shown that the virus may surpasses the blood-brain-barrier through the direct interaction of S1 region of the Spike protein with the Ace-2 molecules on microvascular endothelial cells (Rhea *et al.* 2021), raising also the discussion on the impact of soluble spike protein in the brain. In this sense, the relevance of glutamatergic synapses for appropriate brain function is fundamental, as more than 90% of excitatory synapses are mediated by glutamate ionotropic and metabotropic receptors. Due to its importance, glutamate is constantly recycled within the cell, either as a neurotransmitter, and transported to pre-synaptic vesicles by vesicular glutamate transporters (Vglut) or following its conversion from glutamine to glutamate and then to alpha-ketoglutarate to fuel the TCA cycle during anaplerosis (Gkini and Namba 2022; Andersen *et al.* 2021b). This conversion is essential and happens extensively in astrocytes and neurons through the function of glutaminase. Of note, conversion from glucose and glutamine is the major source of glutamate in the brain, as very little is absorbed from the blood circulation. During certain circumstances, this balance may shift from one side to another, such as during infection or neurodegenerative diseases (Andersen *et al.* 2021a). Thus, the balance between glutamate and glutamine plays a pivotal role in both synaptic transmission and energy acquisition for proper neuronal activity, shifting from vesicular neurotransmission to anaplerosis.

Here we showed that SARS-CoV-2 replication in hamster glial cells significantly changes the levels of several metabolites of importance for brain function, as lactate, glutamine, and alpha-ketoglutarate, as assessed by metabolomics. This is corroborated by our findings with human

astrocytes (Crunfli *et al.* 2020). Also, glucose and TCA cycle components were reduced, whereas viral replication increases along with cytokine secretion. However, here we show that along with increased glycolysis, astrocyte infection with SARS-CoV-2, also used glutamine as a source of carbon. Unexpectedly, however, viral replication in astrocytes was independent of glycolysis, as 2-DG treatment did not impact viral replication, whereas SARS-CoV-2 replication depended on glutamine, as the blockade of glutaminolysis with 6-Diazo-5-oxo-L-norleucine (DON) significantly reduced viral replication and, consequently, the production of inflammatory cytokines. This is in agreement with a detailed previous work that performed a deep metabolomic analysis on the plasma of COVID-19 patients. The authors showed that increased levels of circulating mannose and of glutaminolysis correlated with higher disease severity and viral replication, respectively (Krishnan *et al.* 2021). This is corroborated by a decreased labeling of metabolites of the TCA cycle derived from U¹³-Glutamine, probably caused by a reduction of the oxidative cycle (Mullen *et al.* 2021). Recent other reports have also showed that SARS-CoV2 infection alters the expression of many TCA cycle proteins, as well as their metabolites in lung epithelial cells (Thai *et al.* 2015) and monocytes (Krishnan *et al.* 2021). Thus, it seems clear that SARS-CoV-2 impacts the overall status of protein expression, specifically of those involved in carbon and energy metabolism, and it is than reasonable to speculate that these changes may directly impact brain function, resulting in neurological impairment.

Among the symptoms observed in patients with long-covid or PASC are cognitive impairment, memory loss, and confusion (Whitaker *et al.* 2022). Conversely, hippocampal glutamatergic neurons as well as a balanced concentration of glutamate or amino acid transporters in the synapses are pivotal for concentration, long term potentiation and memory (Centonze *et al.* 2010). Thus, it makes sense that during COVID-19, glutamine consumption due to viral hijacking

Accepted Article

of cellular metabolism may affect glutamate/glutamine balance, and thus leading to the neurological symptoms mentioned, which have already been discussed (Bharadwaj *et al.* 2021). It has been demonstrated that SARS-CoV-2 changes the expression of excitatory amino acid transporters as SLC1A3, important for the recapture of synaptic glutamate, in astrocytes of deceased COVID-19 patients (Yang *et al.* 2021). Also, glutamine may actively participate as a neurotransmitter being provided by perisynaptic astrocytes via Connexin 43 (Cx43). Conversely, Cx43 deficient mice have impaired recognition memory, which was restored after specific recombinant adenoviral vector treatment (AAV-GFAP-Cx43). Similar findings were observed in the cortex and hippocampus of 5xFAD mice, the murine model of Alzheimer's disease (Andersen *et al.* 2021c). Corroborating this hypothesis, a recent case report investigated a 29 years old COVID-19 patient that developed transient attention deficit and memory problems. Magnetic Resonance Spectroscopy (MRS) for the analysis of glutamate, glutamine and N-acetyl aspartate clearly showed a reduction of these molecules in the dorso-lateral prefrontal cortex (DLPFC). Interestingly, three months after infection, neurological impairment has stopped, and glutamate/glutamine levels were reestablished (Yesilkaya *et al.* 2021). Noteworthy to mention that we have observed both viral genome and intense cytokine production in the cortex of infected hamsters *in vivo*.

Thus, to our knowledge, this is the first report to demonstrate the impact of COVID-19 over the metabolic and proteomic profile of brain cells, and more specifically on astrocytes. Moreover, we show that SARS-CoV-2 benefits from glutamine as an important source of energy, which in fact has already been shown for vaccinia virus (Fontaine *et al.* 2014) and cytomegalovirus (Chambers *et al.* 2010) and even SARS-CoV-2 (Krishnan *et al.* 2021), although with distinct cellular populations. Although one weakness of our work is the acute disease model and the lack

of behavioral tests, a recent report in human patients have shown that subacute neurological impairment onset may occur as soon as 16 days (Matos *et al.* 2021). Moreover, our proteomic analysis of hamster's brains *in vivo* compared to human single cell RNA sequencing datasets corroborates the importance of the metabolic and energetic imbalance of glutamate/glutamine that may take place in the brain of neurological COVID-19 patients. Our data brings attention not only to the physiology of the COVID-19 brain, but also suggests that glutamate/glutamine signaling is pivotal, and may be considered either a prognostic factor or a target of specific therapies in patients that develop the neurological impairments observed during long-covid and PASC, as memory loss and cognitive decline, and as already discussed elsewhere (Marinescu *et al.* 2020).

REFERENCES

1. Audi, A. *et al.* Seasonality of Respiratory Viral Infections: Will COVID-19 Follow Suit? *Front. Public Heal.* **8**, 1–8 (2020).
2. Wu, F. *et al.* A new coronavirus associated with human respiratory disease in China. *Nature* (2020) doi:10.1038/s41586-020-2008-3.
3. Guan, W.-J. *et al.* Clinical Characteristics of Coronavirus Disease 2019 in China. *N. Engl. J. Med.* 1–13 (2020) doi:10.1056/NEJMoa2002032.
4. Zhou, P. *et al.* A pneumonia outbreak associated with a new coronavirus of probable bat origin. *Nature* (2020) doi:10.1038/s41586-020-2012-7.
5. Barton, L. M., Duval, E. J., Stroberg, E., Ghosh, S. & Mukhopadhyay, S. COVID-19 Autopsies, Oklahoma, USA. *Am. J. Clin. Pathol.* 1–9 (2020) doi:10.1093/ajcp/aqaa062.
6. Lu, R. *et al.* Genomic characterisation and epidemiology of 2019 novel coronavirus: implications for virus origins and receptor binding. *Lancet* **6736**, 1–10 (2020).
7. Pinto, B. G. G. *et al.* ACE2 expression is increased in the lungs of patients with comorbidities associated with severe COVID-19. *J. Infect. Dis.* **222**, 556–563 (2020).
8. Chu, H. *et al.* Host and viral determinants for efficient SARS-CoV-2 infection of the human lung. *Nat. Commun.* **12**, 1–15 (2021).
9. Chen, R. *et al.* The Spatial and Cell-Type Distribution of SARS-CoV-2 Receptor ACE2 in the Human and Mouse Brains. *Front. Neurol.* **11**, (2021).

10. Hoffmann, M. *et al.* SARS-CoV-2 Cell Entry Depends on ACE2 and TMPRSS2 and Is Blocked by a Clinically Proven Article SARS-CoV-2 Cell Entry Depends on ACE2 and TMPRSS2 and Is Blocked by a Clinically Proven Protease Inhibitor. 271–280 (2020) doi:10.1016/j.cell.2020.02.052.
11. Finkel, Y. *et al.* The coding capacity of SARS-CoV-2. *Nature* **589**, 125–130 (2021).
12. Wu, J. *et al.* SARS-CoV-2 ORF9b inhibits RIG-I-MAVS antiviral signaling by interrupting K63-linked ubiquitination of NEMO. *Cell Rep.* **34**, 108761 (2021).
13. Nasirudeen, A. M. A. *et al.* RIG-i, MDA5 and TLR3 synergistically play an important role in restriction of dengue virus infection. *PLoS Negl. Trop. Dis.* **5**, (2011).
14. Yin, X. *et al.* MDA5 Governs the Innate Immune Response to SARS-CoV-2 in Lung Epithelial Cells. *Cell Rep.* **34**, (2021).
15. Tay, M. Z., Poh, C. M., Rénia, L., MacAry, P. A. & Ng, L. F. P. The trinity of COVID-19: immunity, inflammation and intervention. *Nat. Rev. Immunol.* **20**, 363–374 (2020).
16. Veras, F. P. *et al.* SARS-CoV-2-triggered neutrophil extracellular traps mediate COVID-19 pathology. *J. Exp. Med.* **217**, (2020).
17. Wauters, E. *et al.* Discriminating mild from critical COVID-19 by innate and adaptive immune single-cell profiling of bronchoalveolar lavages. *Cell Res.* (2021) doi:10.1038/s41422-020-00455-9.
18. Gupta, A. *et al.* Extrapulmonary manifestations of COVID-19. *Nat. Med.* **26**, 1017–1032 (2020).
19. Gerkin, R. C. *et al.* Recent smell loss is the best predictor of COVID-19 among individuals with recent respiratory symptoms. *Chem. Senses* **46**, 1–12 (2021).
20. Meinhardt, J. *et al.* Olfactory transmucosal SARS-CoV-2 invasion as a port of central nervous system entry in individuals with COVID-19. *Nat. Neurosci.* **24**, 168–175 (2021).
21. Mao, L. *et al.* Neurologic Manifestations of Hospitalized Patients with Coronavirus Disease 2019 in Wuhan, China. *JAMA Neurol.* **77**, 683–690 (2020).
22. Remsik, J. *et al.* Inflammatory Leptomeningeal Cytokines Mediate COVID-19 Neurologic Symptoms in Cancer Patients. *Cancer Cell* **39**, 276-283.e3 (2021).
23. Al-Mufti, F. *et al.* Acute Cerebrovascular Disorders and Vasculopathies Associated with Significant Mortality in SARS-CoV-2 Patients Admitted to The Intensive Care Unit in The New York Epicenter. *J. Stroke Cerebrovasc. Dis.* **30**, 105429 (2021).
24. Rehmani, R., Segan, S., Maddika, S. R., Lei, Y. W. & Broka, A. Spectrum of neurologic & neuroimaging manifestation in COVID-19. *Brain, Behav. Immun. - Heal.* **13**, 100238

(2021).

25. Fragiel, M. *et al.* Incidence, clinical, risk factors and outcomes of Guillain-Barré in Covid-19. *Ann. Neurol.* **89**, 598–603 (2021).
26. Del Brutto, O. H. *et al.* Cognitive decline among individuals with history of mild symptomatic SARS-CoV-2 infection: A longitudinal prospective study nested to a population cohort. *Eur. J. Neurol.* 1–9 (2021) doi:10.1111/ene.14775.
27. Eskandar, E. N. *et al.* Neurologic Syndromes Predict Higher In-Hospital Mortality in COVID-19. *Neurology* **96**, e1527–e1538 (2021).
28. Nagu, P., Parashar, A., Behl, T. & Mehta, V. CNS implications of COVID-19: A comprehensive review. *Rev. Neurosci.* **32**, 219–234 (2021).
29. Hao, Y. *et al.* Integrated analysis of multimodal single-cell data. *Cell* **184**, 3573–3587.e29 (2021).
30. Hafemeister, C. & Satija, R. Normalization and variance stabilization of single-cell RNA-seq data using regularized negative binomial regression. *bioRxiv* 1–15 (2019) doi:10.1101/576827.
31. Ahlmann-Eltze, C. & Huber, W. glmGamPoi: Fitting Gamma-Poisson generalized linear models on single cell count data. *Bioinformatics* **36**, 5701–5702 (2020).
32. Finak, G. *et al.* MAST: A flexible statistical framework for assessing transcriptional changes and characterizing heterogeneity in single-cell RNA sequencing data. *Genome Biol.* **16**, 1–13 (2015).
33. Jiang, J., Wang, C., Qi, R., Fu, H. & Ma, Q. scREAD: A Single-Cell RNA-Seq Database for Alzheimer's Disease. *iScience* **23**, 101769 (2020).
34. Mi, H. *et al.* Protocol Update for large-scale genome and gene function analysis with the PANTHER classification system (v.14.0). *Nat. Protoc.* **14**, 703–721 (2019).
35. Eymieux, S. *et al.* Ultrastructural modifications induced by SARS-CoV-2 in Vero cells: a kinetic analysis of viral factory formation, viral particle morphogenesis and virion release. *Cell. Mol. Life Sci.* **78**, 3565–3576 (2021).
36. Imai, M. *et al.* Syrian hamsters as a small animal model for SARS-CoV-2 infection and countermeasure development. *Proc. Natl. Acad. Sci. U. S. A.* **117**, 16587–16595 (2020).
37. Wang, L. *et al.* Progress in Research on SARS-CoV-2 Infection Causing Neurological Diseases and Its Infection Mechanism. *Front. Neurol.* **11**, 1–9 (2021).
38. Piras, I. S. *et al.* Anti-brain antibodies are associated with more severe cognitive and behavioral profiles in Italian children with Autism Spectrum Disorder. *Brain. Behav.*

Immun. **38**, 91–9 (2014).

39. Bharadwaj, S., Singh, M., Kirtipal, N. & Kang, S. G. SARS-CoV-2 and Glutamine: SARS-CoV-2 Triggered Pathogenesis via Metabolic Reprogramming of Glutamine in Host Cells. *Front. Mol. Biosci.* **7**, 1–14 (2021).
40. Codo, A. C. *et al.* Elevated Glucose Levels Favor SARS-CoV-2 Infection and Monocyte Response through a HIF-1 α /Glycolysis-Dependent Axis. *Cell Metab.* **32**, 437–446.e5 (2020).
41. Thai, M. *et al.* MYC-induced reprogramming of glutamine catabolism supports optimal virus replication. *Nat. Commun.* **6**, 1–9 (2015).
42. Centonze, D. *et al.* The link between inflammation, synaptic transmission and neurodegeneration in multiple sclerosis. *Cell Death Differ.* **17**, 1083–91 (2010).
43. Yang, A. C. *et al.* Dysregulation of brain and choroid plexus cell types in severe COVID-19. *Nature* **595**, 565–571 (2021).
44. Yesilkaya, U. H., Sen, M. & Balcioglu, Y. H. COVID-19-related cognitive dysfunction may be associated with transient disruption in the DLPFC glutamatergic pathway. *J. Clin. Neurosci.* **87**, 153–155 (2021).
45. Fontaine, K. A., Camarda, R. & Lagunoff, M. Vaccinia Virus Requires Glutamine but Not Glucose for Efficient Replication. *J. Virol.* **88**, 4366–4374 (2014).
46. Chambers, J. W., Maguire, T. G. & Alwine, J. C. Glutamine Metabolism Is Essential for Human Cytomegalovirus Infection. *J. Virol.* **84**, 1867–1873 (2010).
47. Marinescu, I., Marinescu, D., Mogoantă, L., Efrem, I. C. & Stovicek, P. O. Sars-cov-2 infection in patients with serious mental illness and possible benefits of prophylaxis with memantine and amantadine. *Rom. J. Morphol. Embryol.* **61**, 1007–1022 (2020).

Figure Legends

Figure 1. SARS-CoV-2 infects and replicates in astrocyte cultures. SARS-CoV-2 spike protein (red) was identified in astrocytes cultures Presence of SARS-CoV-2 spike protein in uninfected (A) and infected astrocytes (MOI 1) at 72 hpi (B and C). Viral RNA (D) and infectious particles (E) were detected in astrocytes infected with MOI 0.1 by qPCR and PFU assay, respectively. Statistical analysis were performed by One-way ANOVA. Correlation plots comparing SARS-CoV-2 subgenomic RNA and genomic RNA CTs (F). Regression line for each time point indicated

95% confidence area shown in shaded areas. Spearman's correlation coefficient and associated p-values are shown. Transmission electron microscopy of astrocytic cultures infected with MOI 0.1 at 72 hpi (E). Black arrows indicates SARS-CoV-2 particles attached to the cell surface and red asterisks indicates double-membrane vesicles. The data is representative of three experiments. Experimental replicates: 0, 24, 48, and 72hpi, n= 6 (D); 24 and 72hpi, n=3 (E), 0, 24, 48, and 72hpi, n = 5 (F). n = number of independent cell culture preparations. Statistical information: (DF total, 23; F, 25,7; p-value <0,0001) (D) and t-tests (DF, 4; t-value, 16,07; p-value, <0,0001). **Figure 2. SARS-CoV-2 induces pro-inflammatory cytokines, interferon stimulated genes expression and protein alterations in hamsters' primary astrocytes.** Principal component analysis of infected and uninfected cultures proteomic data (A). Quantitative PCR for pro-inflammatory (B-D) and interferon stimulated genes (E-H) of cultures infected with SARS-CoV-2 MOI 0.1. Fold change is the relative expression of infected to control cultures. Statistical analyses were performed by t-test and $p < 0.05$ was considered significant. Heatmap of proteomic analysis from cultures infected with SARS-CoV-2 MOI 0.1. n=8 for infected and n=10 for control samples (I). Color density represents the protein z-score. DEPs from proteomic data submitted to KEGG database analysis (J). The nodes in gray represent major pathways and the color of the genes the z-score (red to blue). Experimental replicates: CTRL, n= 8; CoV-2, n = 9 (A, I and J) CTRL, n=3; CoV-2, n = 3 (B-H). The data is representative of two independent experiments.

Figure 3. SARS-CoV-2 infection alters mitochondrial morphology, reactive oxygen species production and cellular bioenergetics of hamsters's astrocytes cultures. Mitochondrial related analysis were performed after SARS-CoV-2 infection (MOI 0.1) at 72 hpi. Mitochondrial morphological changes were evidenced by TEM (scale bar 200nm) (A). Statistical analysis were performed by t-test. Mitochondrial ROS production was measured by flow cytometry at 24- and

72 hpi, graphs represent median intensity fluorescence (MFI) (B). Statistical analysis were performed by two-way ANOVA followed by Sydak's multiple comparisons post-hoc test. Bioenergetic profile by oxygen consumption rate (OCR) (C) and extracellular acidification rate (ECAR) of infected cells at 72 hpi (D). Statistical analysis were performed by t-test. Statistical significance: $p < 0.05$. Experimental replicates: CTRL, $n = 3$; CoV-2, $n = 3$ (B). CTRL, $n = 3$; CoV-2, $n = 4$ (C and D) Data are representative of two independent experiments.

Figure 4. SARS-CoV-2 impacts hamsters' astrocytes metabolic pathways. Targeted metabolomic data of glycolysis (A-C), TCA cycle (K), fatty acid (E and F) and glutamate related metabolites (H, I K and M) of hamsters' astrocytes cultures infected or not with SARS-CoV-2 at MOI 0.1. The arrows represent the relationship between metabolites. The analysis was conducted at 72 hpi (MOI 0.1) and data is represented by the area under the curve of each metabolite detection peak. Statistical analysis were performed by Welch's t-test and $p < 0.05$ was considered significant. Experimental replicates: CTRL, $n = 9$; CoV-2, $n = 9$.

Figure 5. Blockade of glutaminolysis reduces SARS-CoV-2 replication and pro-inflammatory gene expression. Illustration showing the targets of 2-DG, Etomoxir, and DON blocking glycolysis, β -oxidation and glutaminolysis, respectively (A). Cell viability following 72h treatment with 2-DG (0,05-500mM), Etomoxir (0,03-300 μ M) and DON (0,05-500 μ M) (B). Cultures were pre-treated with 2-DG (5mM), Etomoxir (3 μ M) and DON (50 μ M) 2 hours prior to SARS-CoV-2 infection (MOI 0.1). Viral RNA and infectious particles were quantified after 72 hpi by qPCR (C) and PFU (D). Viral RNA of cultures supplemented or not with glucose (17mM) or glutamine (2 mM) (E). qPCR of pro-inflammatory and interferon stimulated genes from cultures treated with DON (F-L). Statistical analysis were performed by multiple t-test (C) or one-way

ANOVA with Tukey's multiple comparisons (D-L). Cultures were performed in triplicates and graphs representative of two experiments.

Figure 6. SARS-CoV-2 infects Syrian hamsters' brains in vivo and elicit changes comparable to the human disease. The animals were inoculated intranasally with 10⁵ TCID of SARS-CoV-2 and viral RNA detection was performed by qPCR in different areas of the brain over the infection course (A). Cytokine expression by qPCR (B and D) and KEGG pathways analysis (C and E) of mock or infected hippocampus and cortex, respectively at 72 dpi. The fold change was normalized by the relative expression of uninfected groups and only significant DEPs (FDR adjusted) were included in the KEGG analysis. Statistical analysis in gene expression graphs were performed by t-test and p<0.05 was considered significant. Illustrative scheme of data generation from the comparison of our hamster proteomic data to human data set (F). The generated data were fed into an alluvial graph connecting the DEPs from hamster brain proteomics with significant ontology pathways of public human brain single-cell sequencing data sorted by specific brain cell populations (G). Experimental replicates: 3dpi, n= 5; 5dpi, n = 5; 7dpi, n = 4; 14dpi, n =3 (A) Mock, n= 5 and CoV-2 n=6 (B-E). OPC = Oligodendrocyte progenitor cell. Graphs are representative of two experiments.

Figure 7. SARS-CoV-2 impacts metabolic and protein profile of brain and primary mixed glial cells from Syrian hamsters: a glimpse for SARS-CoV-2 induced neurological disorders during long COVID-19. The presence of SARS-CoV-2 within different regions (olfactory bulb, hippocampus and cortex) of infected Syrian hamster's brain suggests that the virus might reach the central nervous system. As well as during astrocytes in vitro infection, the infection of SARS-CoV-2 is associated with increased expression of pro-inflammatory cytokines (Il-6, Il-1b, Tnfa) and interferon stimulated genes (Ace-2, Isg20, Ifm3) (A) Astrocytes infected in vitro also

demonstrated dysregulated metabolic pathways such as mitochondrial respiration and glycolysis associated with an important decrease of intermediates and substrates from tricarboxylic cycle (TCA) (B). Importantly, the blockage of glutaminolysis was critical for the maintenance of viral replication (C). Finally, protein analysis evidenced that SARS-CoV-2 infection in both in vitro and in vivo results in enriched pathways associated with neurological diseases and alterations in inflammatory and metabolic pathways which are also found in single cell analysis of COVID-19 patients' brains.

Funding Support

This study was funded by Fundação de Amparo à Pesquisa do Estado de São Paulo (FAPESP) grants to JPSP (#2017/26270-0 and #2020/06145-4), DMS (#19/25957-2 and #17/25588-1), AMMSG (#2020/07251-2), PMCM (2017/27131-9), PMMM (2015/15626-8; 2020/04579-7), DMF (#2015/25364-0), JBS grant to MRDIL (FUSP Agreement 3558). Fellowships to CMP (#2017/11828-0), NGZ (#2019/12431-2), MGO (#2019/12431-2), MCA (#2019/12691-41), CLS (#2019/13916-0); AMMSG AFSF fellowship: 2020/09149-0; TTSP fellowship: CAPES 88887.508739/2020; MRDIL (CNPq 303810/20181). JPSP is recipient of a G4 grant from Institut Pasteur (FUSP-Pasteur 3303-01) and CNPq (#316646/2021-0). LGO and YSA are recipients of CAPES fellowship.

Acknowledgements

We would like to thank all the members of the Neuroimmune Interactions Laboratory, the Scientific Platform Pasteur-USP and the Laboratory of Neuroproteomics for discussions and suggestions. CNPEN/LNaNo personnel for the support with the TEM images. This research used facilities of the Brazilian Nanotechnology National Laboratory (LNNano), part of the Brazilian

Centre for Research in Energy and Materials (CNPEM), a private non-profit organization under the supervision of the Brazilian Ministry for Science, Technology, and Innovations (MCTI). The LNNanostaff is acknowledged for the assistance during the experiments (proposal # TEM-27105F.). We also would like to thank Prof. Claudio Romero Marinho and Prof. Carsten Wrenger of the Department of Parasitology ICB-USP for giving us access to the BSL-3 facility. No thanks to the Brazilian federal government, whose huge financial cuts make Brazilian science to agonize.

Author's Contribution

LGO and YSA designed and performed all *in vitro* and *in vivo* experiments and analyzed data; PY performed *in vitro* experiments, VCC, FC, GRS and LC performed the proteomics and metabolomics and analyzed the data; EDA and NBS performed immunofluorescence and analyzed the data, GMA, EMF, IMP performed the experiments with brain slices, CMP, NGZ, MGO helped with all *in vitro* experiments; EGC performed TEM; PS performed all bioinformatics analyses; GGD performed *in vitro* respirometry and analyzed data; MCA, CLS, AFSF, MVA and TTSP performed *in vivo* infection, ACAC and LGBG helped isolating SARS-CoV2, MPC helped isolating the virus and sequenced the viral genome; MRL, DMF and AMMSG provided *in vivo* samples and reagents from infected animals and edited the manuscript; PCM provided materials and reagents and edited the manuscript; CDM provided reagents for immunofluorescence and analyzed data; CMCM provided animals and reagents; PMMV provided reagents for respirometry, analyzed data and edited the manuscript; TMC provided reagents and performed the brain slice experiments, analyzed data and discussed the manuscript; DMS provided reagents and performed proteomics and metabolomics, analyzed the data, and edited the manuscript; JPSP designed and supervised the project, analyzed data and wrote the manuscript.

Figure 1:

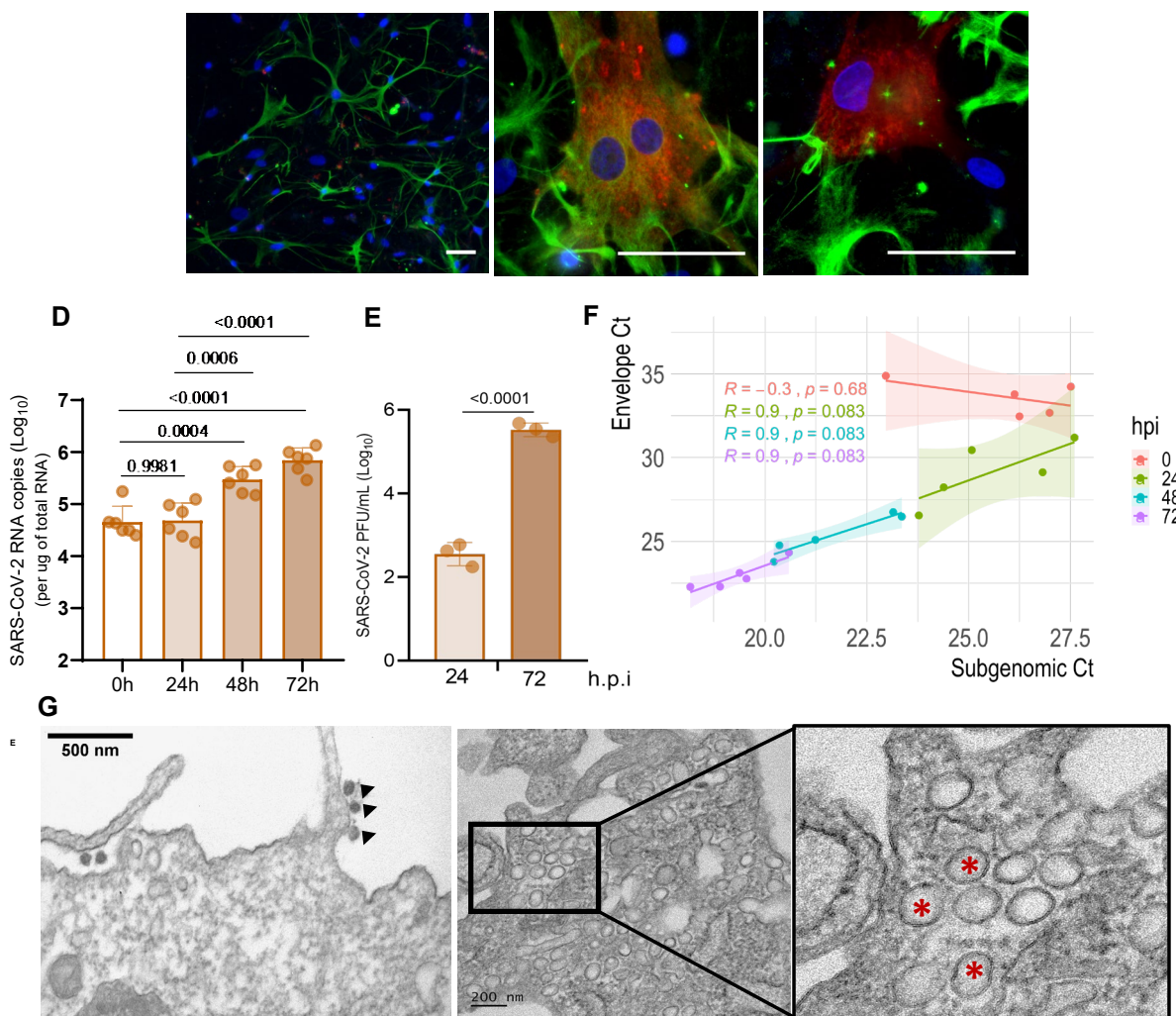
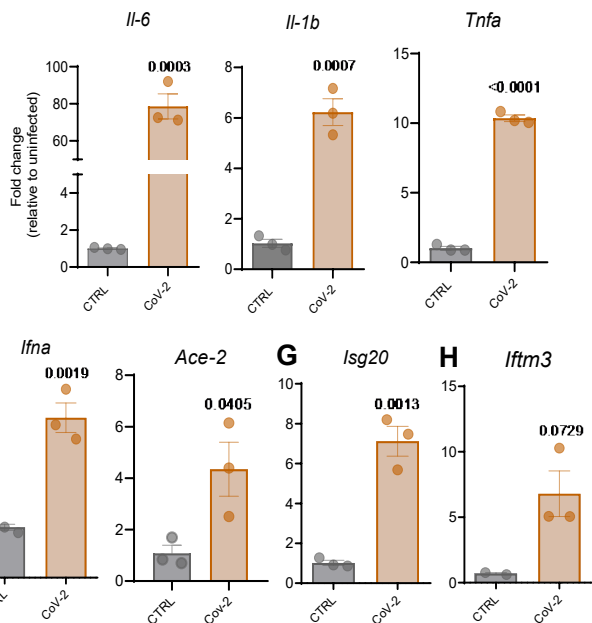
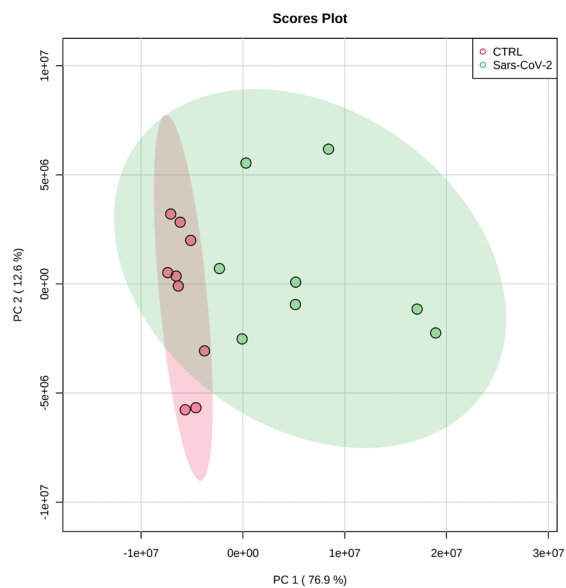
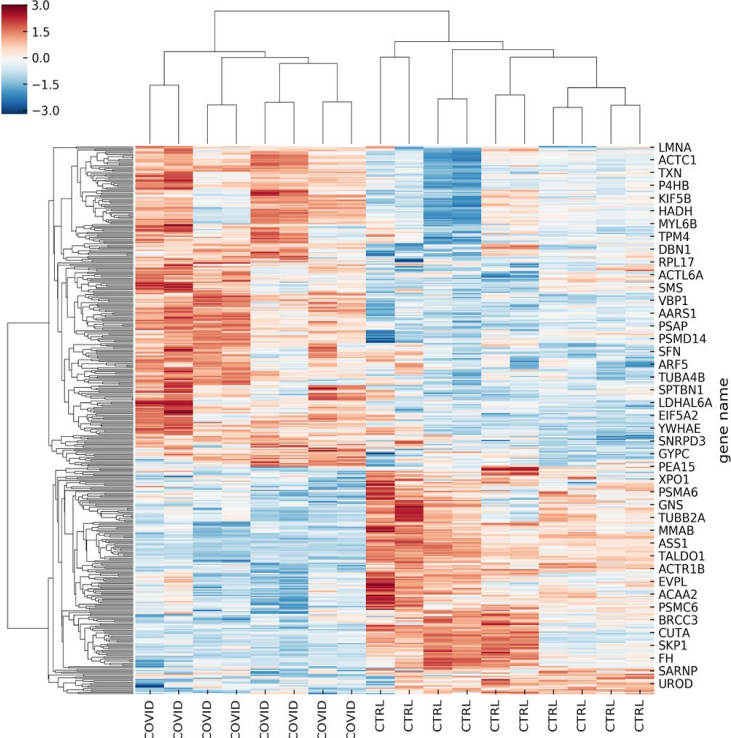
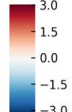


Figure 2:



CTRL vs COVID



Pathways dysregulated in SARS-COV-2

Database: KEGG

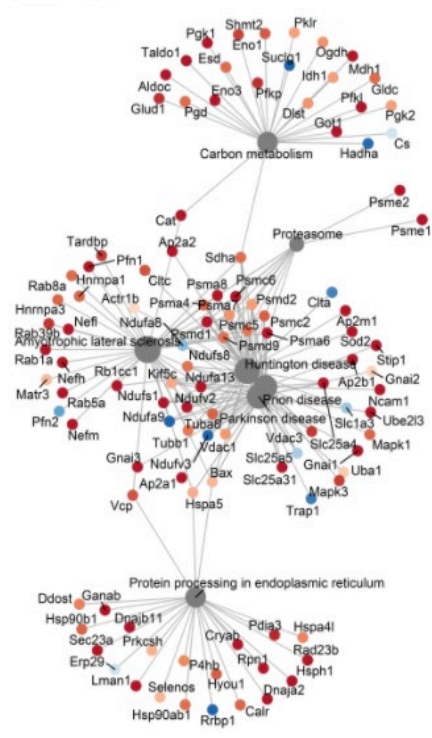


Figure 3:

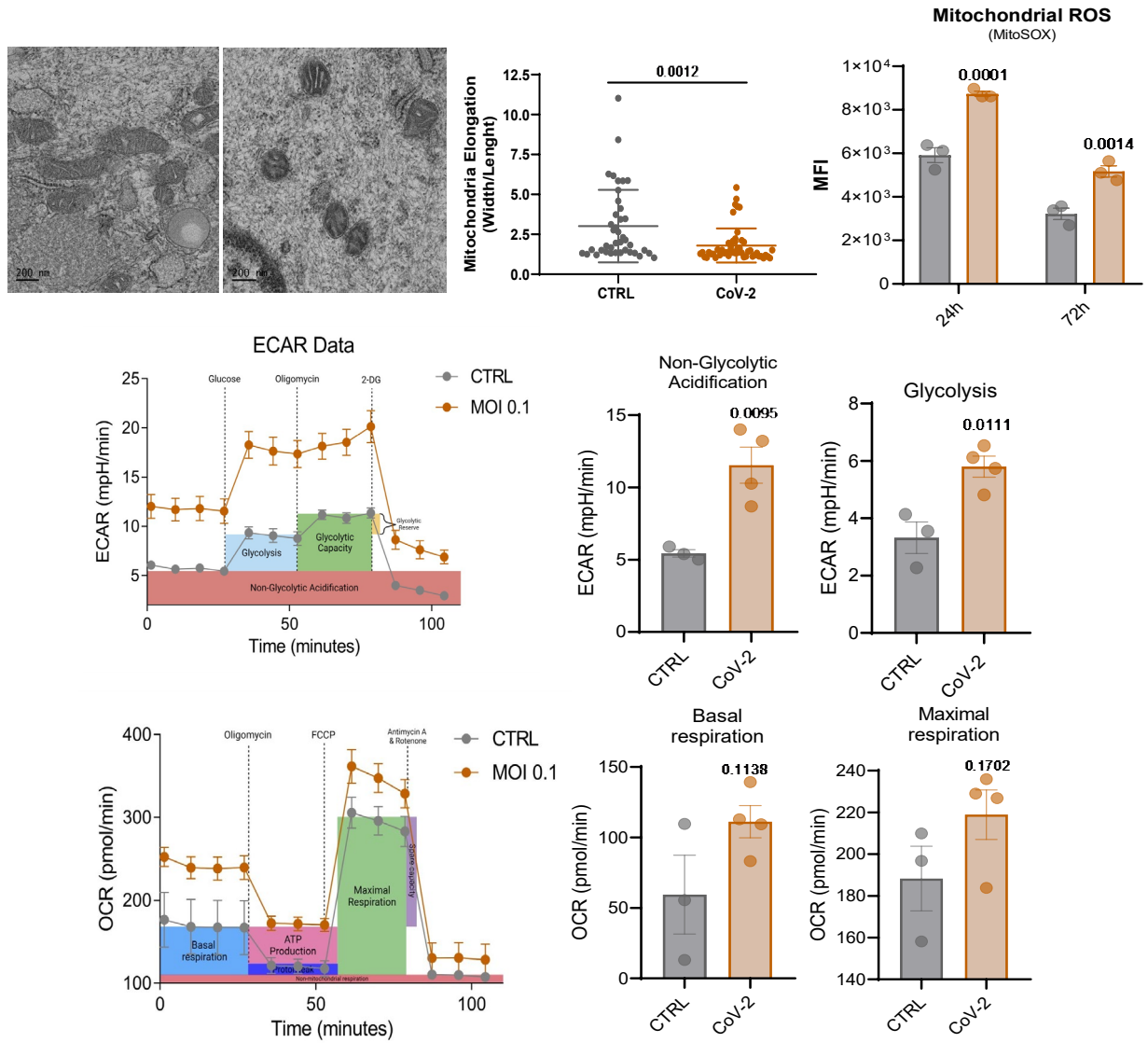


Figure 4:

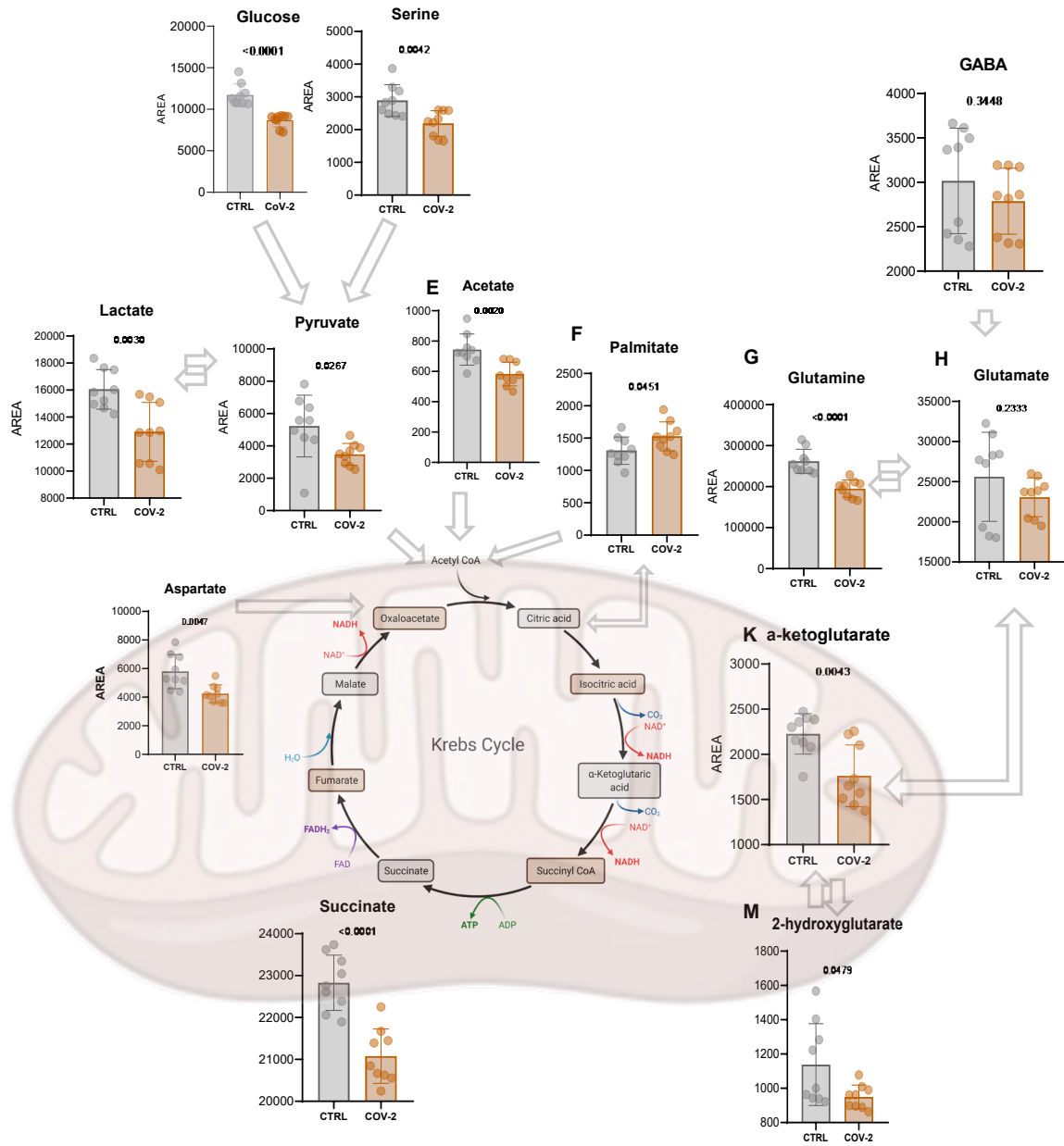
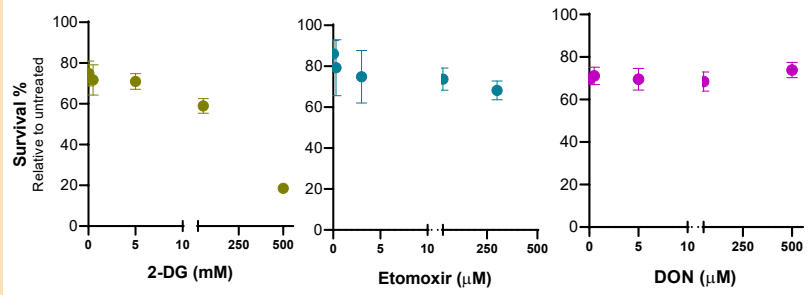
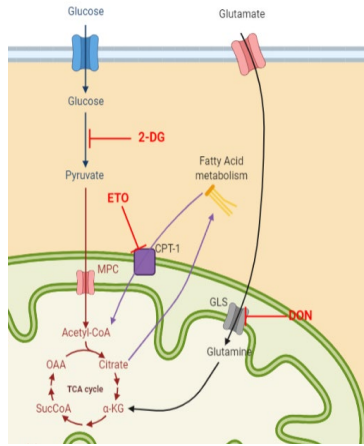


Figure 5:



● CoV-2 ● CoV-2 + 2-DG ● CoV-2 + Etomoxir ● CoV-2 + DON

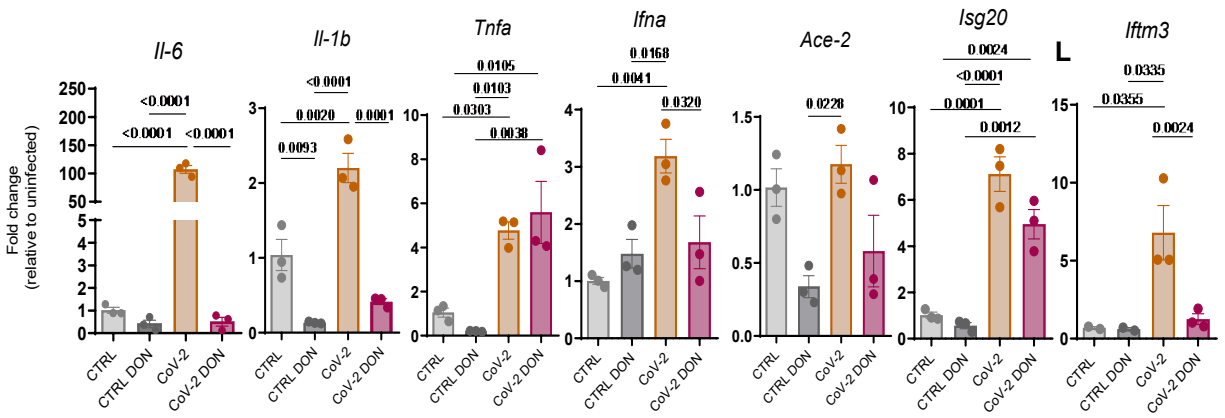
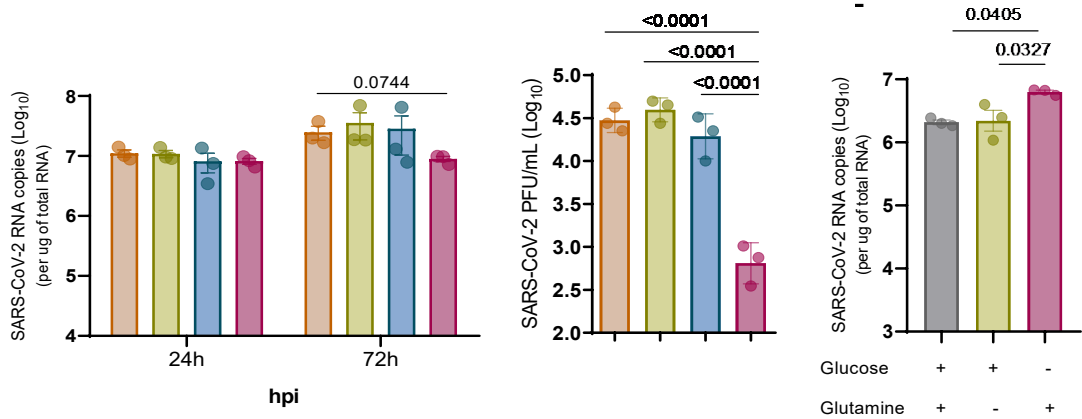


Figure 6:

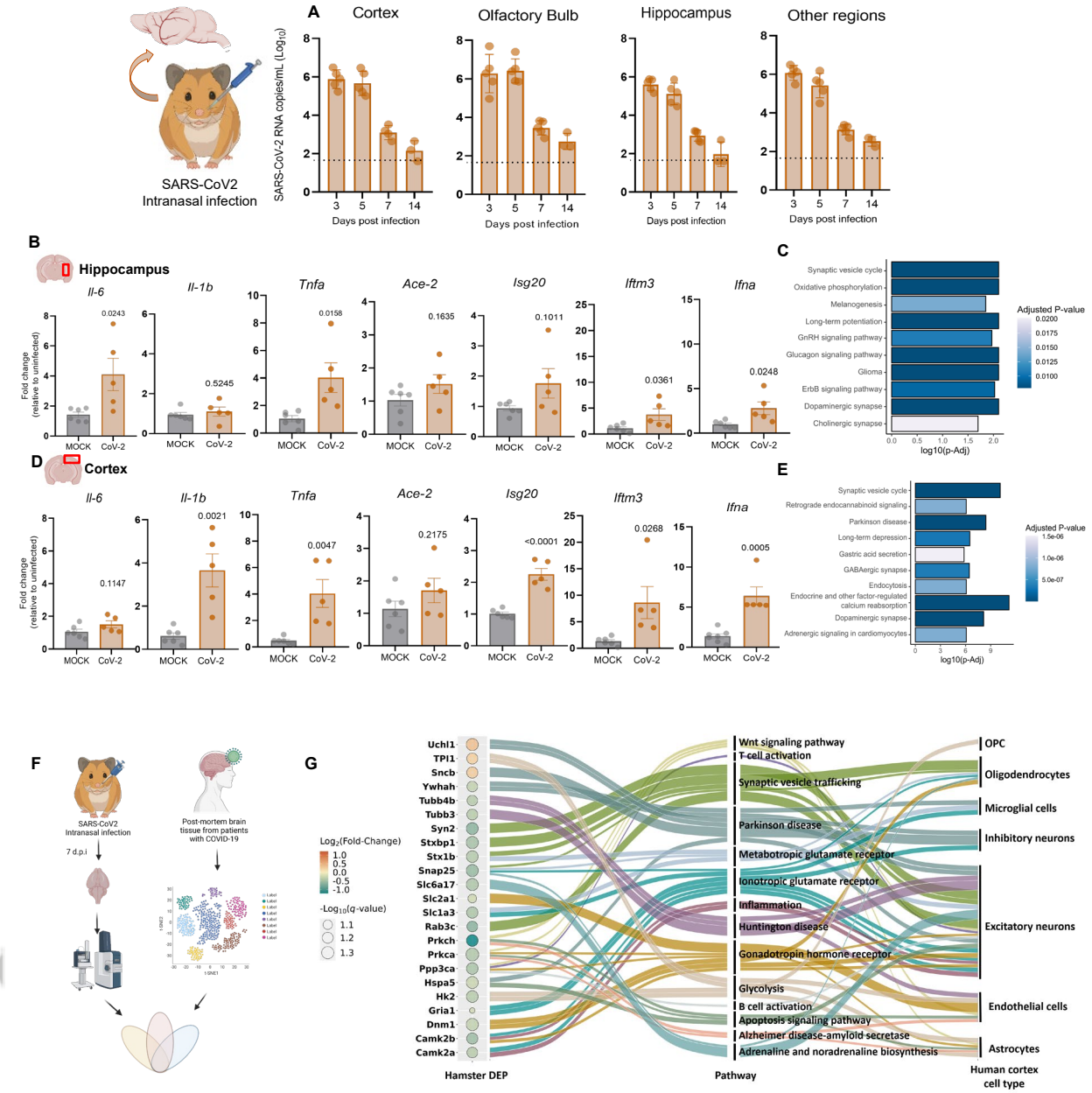
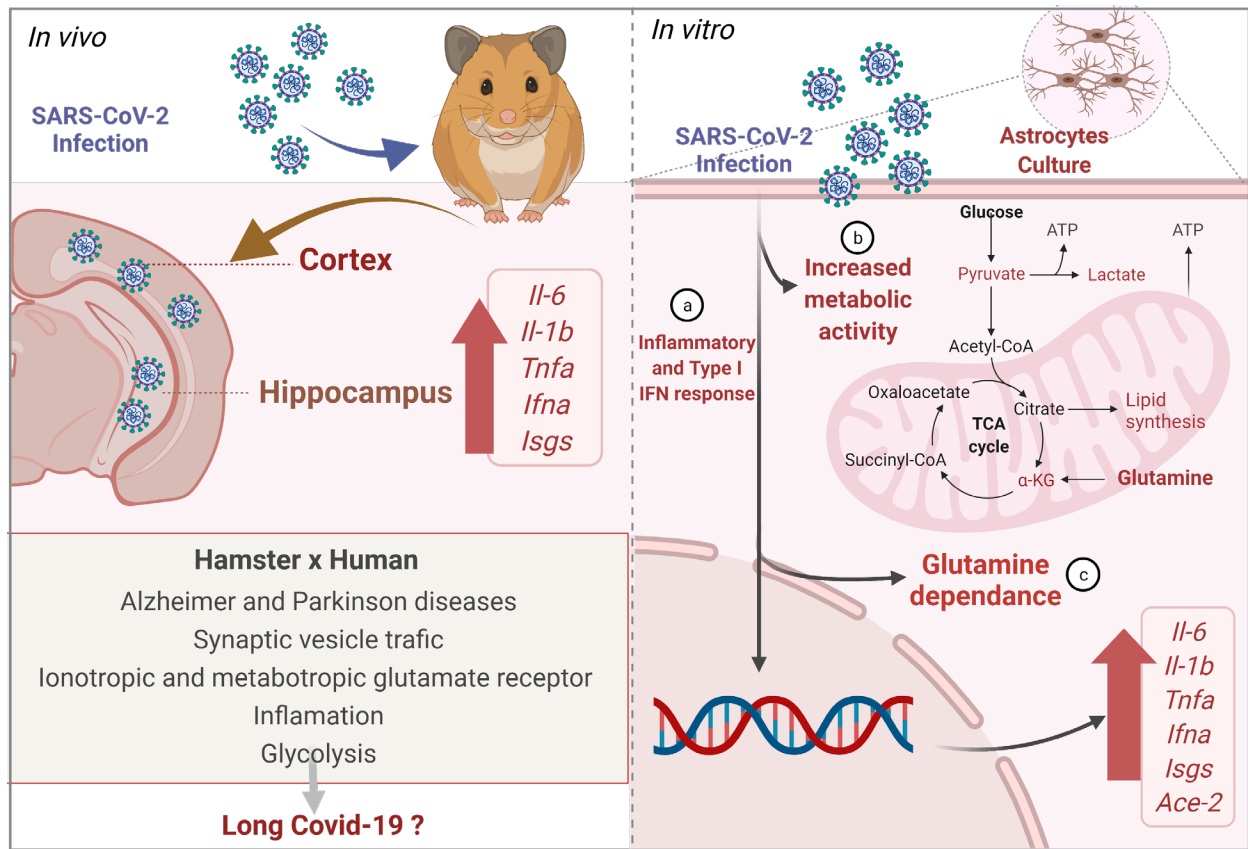


Figure 7: Graphical abstract



- SARS-CoV-2 infects hamsters' astrocytes and alters carbon metabolism protein expression
- SARS-CoV-2 replication in astrocytes depends on glutamine
- Metabolomics analysis evidences intense metabolic activation and metabolites consumption
- SARS-CoV-2 is detected in the cortex and hippocampus in intranasally infected hamsters
- Bioinformatics comparisons with hamsters proteomics and human COVID-19 brain samples evidence an overlap of altered proteins related to metabolism and synapses.